μXRF INVESTIGATION OF RELATIONSHIPS BETWEEN GEOCHEMISTRY AND PHYSICAL GRAIN CHARACTERISTICS IN GLACIO-FLUVIAL-AEOLIAN CATCHMENTS IN SOUTHWEST & NORTHWEST ICELAND

A Thesis

by

EMILY SHAE DYE

Submitted to the Graduate and Professional School of
Texas A&M University
in partial fulfillment of the requirements for the degree of

MASTER OF SCIENCE

Chair of Committee,	Ryan Ewing
Committee Members,	Michael Tice
	Youjun Deng
	Marion Nachon
Head of Department,	Julie Newman

December 2022

Major Subject: Geology

ABSTRACT

In order to determine how sediment transport and alteration processes change the composition of sediment relative to source rock, Icelandic, basaltic fluvial and aeolian sediments were analyzed from the Þórisjökull glacial outwash, a mineral dominated sand field, and Jökulsá á Fjöllum fluvial system, a glass dominated field. These areas were investigated as an analog to early Mars, which is thought to have an active hydrologic and sedimentary system involving glacial, fluvial, and aeolian processes in a basaltic landscape. μXRF element maps, geochemical data, grain size, and thin sections were used to characterize how sediment changes through different grain sizes, environments, and increasing distance from the source.

Sedimentologic results showed the 2021 sediments were finer and more angular than 2019 sediments. Geochemical data revealed that grain size and distance from source were primary factors affecting composition and environment of deposition was secondary. Increased transport distance increased range for geochemical oxide results, yet trends could still be seen in a short distance. FeO and MnO increased with increasing grain size, while SiO_2, MgO and CaO decreased with grain size. Other oxides in this study experienced lesser trends than these. The 2021 area contained increased amounts of TiO_2 compared to the 2019 area indicating a glassier source material. The 2021 area also contained larger ranges for weight percent oxides in sediments than the 2019 area indicating more geochemical variation. The μXRF element maps and thin sections detected multimineralic grains in the coarser grain sizes and the enrichment of monomineralic in finer grain sizes yet was not useful for detecting geochemical trends through a transect. Our results show that μXRF on loose sediment for specific use cases can provide valuable geochemical information on both Earth and Mars.

DEDICATION

I dedicate this thesis to my loving husband, Jacob. I love you. John 3:16.

ACKNOWLEDGEMENTS

Through my years at Texas A&M University, I have met an incredible number of people. I would like to use this section to acknowledge the people who have been influential on not only this project, but my life.

First and foremost, I would like to thank my advisor, Dr. Ryan Ewing. Ryan decided to take me on as a freshman undergraduate researcher whose knowledge of geology extended to GEOL 101. I am so grateful that he did as I would not be here today without his trust in me. Ryan has always been the most patient advisor and teacher. He always re-explained concepts and answered questions he's answered 5 times before. I would like to thank him for the opportunity of going to Iceland and obtaining my masters with him. It was one of the best experiences of my life and I gained knowledge I could've never reached just in a classroom.

In addition to Ryan, I would like to thank Dr. Marion Nachon for her mentorship, wisdom, and encouragement. She always sacrificed time to teach me new concepts and train me on μXRF. Her encouragement was always present with a smile, and she inspired me to love geology and learning more. I could not have done this project without the help of Marion. She has taught me things not only about geology, but lessons I will use for the rest of my life.

I would like to acknowledge the SAND-E team as they all played a huge role in the execution of this project and became my friends along the way. Thank you, again, to Ryan Ewing for his leadership. Thank you to Candice Bedford who helped me immensely on geochemistry knowledge and volcanic geology. I would also like to acknowledge Liz Rampe, Kashauna Mason, Lauren Berger, Briony Horgan, Amanda Rudolph, Marion Nachon, Prakhar Sinha, Mike Thorpe,

Mathieu Laporte, Michael Hasson. Thank you to the Mission Control engineers that made SAND-E possible: Evan Smal, Ewan Reid, Melissa Battler, Kaizad Raimalwala, and Adam Deslauriers.

Thank you to the Aeolus lab team for all their feedback, positivity, and friendship. I would like to specifically acknowledge Mike Zawaski as he helped me tremendously towards the end of this project by analyzing the remainder of my samples using the μXRF. He also never failed to help me think critically about my project and answered many of my questions. In addition, thank you to Kashauna Mason for analyzing grain size of all of my samples and organizing SAND-E in the lab. I would also like to acknowledge my committee for their guidance and support through this project: Dr. Ryan Ewing, Dr. Mike Tice, Dr. Youjun Deng, Dr. Marion Nachon. Thank you, specifically to Dr. Mike Tice for the allowing me to use his lab and μXRF through the years.

Additionally, I would like to thank all of my friends at Texas A&M but want to list a few by name as they have been of constant encouragement and love: Leah Evan, Sidney Dangtran, and Lauren Berger. These friends have seen me through thick and thin, yet always pushed me to keep moving forward and not give up. The countless laughs we shared always made doing this thesis a little easier.

Thank you to my loving parents, Daralee and Eric Champion, for always supporting my dream of becoming a geologist and encouraging me along every step of the way. Thank you to my in-laws, Rich and Gayla Dye, for their constant encouragement and love. Finally, I would like to thank the person who ultimately kept me going through this degree, my husband, Jacob. Thank you for your love, patience, encouragement, support, and prayers. I could not have done this project without you. You are the person that pushes me closer to Christ as well as to be the best version of myself.

CONTRIBUTORS AND FUNDING SOURCES

Contributors

This work was supervised by a thesis committee consisting of Professor Ryan Ewing, Michael Tice, and Marion Nachon of the Department of Geology and Geophysics and Professor Youjun Deng of the Department of Soil Science.

The data analyzed for 2021 was provided by Mike Zawaski. The analyses were able to be completed on the μXRF thanks to Dr. Michael Tice. The maps in Fig. 1 were completed by Kashauna Mason and Constantine Stollis.

All other work conducted for the thesis was completed by the student independently.

Funding Sources

Graduate study was supported by the support of NASA Planetary Science and Technology from Analog Research (PSTAR) 80NSSC18K1519`.

This work was also made possible in part by the Mary & Michael Blackwell '73 Endowed Scholarship from the College of Geosciences, Geology and Geophysics.

NOMENCLATURE

PIXL	Planetary instrument for X-ray Lithochemistry
PPL	Plain Polarized Light
SAND-E	Semi-Autonomous Navigation for Detrital Environments
XPL	Crossed Polarized Light
μXRF	Micro X-Ray Fluorescence

TABLE OF CONTENTS

Page

LIST OF FIGURES

LIST OF TABLES

1. INTRODUCTION

Sediment transport and alteration processes change sediment composition relative to the source rock (Young and Nesbitt, 1998; Fralick, 2003; Mangold et al., 2011; Fedo et al., 2015). Though well-studied in quartzofeldspathic systems, less information exists on how sediments derived from basaltic sources change physically and chemically through a transport system. This raises questions about the applicability of quartzofeldspathic-based source-to-sink studies to unique basalatic volcaniclastic systems on Earth and to Mars (Thorpe et al., 2019). This lack of study is due to the limited abundance of basaltic provenances on Earth's surface (Thorpe et al., 2021). Hawaii and Iceland are the most well-known and studied basaltic provinces on Earth and have been the focus of several studies on the physio-chemical changes in basaltic materials.

Studies that have targeted source-to-sink changes in sediments in basaltic provinces have shown both chemical and physical weathering impact the composition of sediments (Mangold et al., 2011; Fedo et al., 2015; Thorpe et al., 2019). Many studies seek to characterize how sediments change in grain sizes and distance from the source in aeolian and fluvial mediums. These studies indicate that chemical weathering is a principal control on the geochemical makeup of sediments in basaltic fluvial environments and the physical sorting of sediments is strongly dependent on grain size and mineral density in fluvial systems (Thorpe et al., 2019). Aeolian basaltic studies show fractionation due to physical sorting in the overall makeup of sediments such as olivine-enrichment relative to source rock (Mangold et al., 2015).

Unlike Earth where basaltic provinces are relatively rare, the rock record on Mars is made up almost entirely of volcaniclastic sedimentary rocks with basaltic compositions (e.g., Malin and Edgett, 2000). Our ability to interpret the rocks and ancient environments on Mars hinges on our

understanding of how basaltic sediments are affected by physical and chemical processes that occur through the sedimentary rock cycle. The ancient rocks of Mars are correlative in time to Earth's earliest sedimentary rocks and because these rocks remain exposed at Mars's surface, they are ideal targets to study the ancient sedimentary environments that potentially hosted life (McLennan & Grotzinger, 2008; Veizer & Jansen, 1985; Thorpe et al., 2021). Environments that are current targets of in situ exploration on Mars include Gale crater, studied by the Curiosity rover, and Jezero crater, by Perseverance rover. Curiosity has a primary goal of characterizing the habitability of ancient and modern environments, while Perseverance has goals of assessing habitability of Mars and detecting preserved biosignatures (Rampe et al., 2020; Farley et al., 2020). Significant questions remain about the type of depositional environments, habitability, and the former presence of life on Mars. By interpreting variations in sediment composition and grain properties in Earth's basaltic environments, a greater understanding of habitability on Mars and constraints can be placed on past sedimentary environments.

Iceland is an ideal analog for Mars. The island is located along the Mid-Atlantic spreading ridge in the North-Atlantic Ocean and composed of complex basaltic volcanic terrains modified by glacial-fluvial-aeolian sedimentary processes (e.g., Arnalds et al., 2001; Gíslason, 2008; Baratoux et al., 2011; Thorpe et al., 2019). It is the basaltic volcaniclastic sediments generated by fluvial and aeolian sedimentary processes, along with cold-climate weathering and alteration processes similar to those found on Mars (late Noachian to early Hesperian period) that make Iceland an ideal analog for sedimentary and geochemical processes on Mars (Carr, 2012; Wordsworth et al., 2015; Achilles et al., 2017; Thorpe et al., 2021). The unique setting of Iceland provides an opportunity to better understand how the physical and geochemical properties of

basaltic, volcaniclastic sediments change from their source terrains as they move through glacial, fluvial, and aeolian transport systems.

This project uses μXRF to understand how sand transported along a basaltic glacio-fluvial-aeolian pathway changes with increasing distance from the source. μXRF was chosen for this project as it allows for both quantitative weight percentage quantification and element map assessment of sediments and is an instrument currently in use on the Mars Perseverance rover (Allwood et al., 2020). μXRF is typically used to study cores and hand samples, rather than loose grains, however one of the motivations behind this project is to expand the use of μXRF to loose sediments and determine trends in composition with grain size and how they relate to source regions (Flude et al., 2017). μXRF is a valuable tool to use for loose sediment analysis when used in partnership with grain size fractions as it can give insight to 1) weight percentage analysis of the sediment, 2) visually identify trends within the sediment, otherwise impossible with just XRF. The Planetary Instrument for X-ray Lithochemistry μXRF is currently deployed at Jezero Crater, Mars onboard the Perseverance rover as part of the Mars 2020 mission.

PIXL was deployed on the NASA Mars 2020 *Perseverance* rover that landed on Mars in February 2021. This instrument was inspired by the desire to correlate rock composition and in situ. Past XRF instruments that have been deployed on past rover missions gather elemental chemistry on bulk rock composition with an average over large areas. With PIXL, greater geochemical detail of rocks can lead to greater discovery. PIXL has three main goals, (1) provide a detailed geochemical analysis of past environments on Mars, (2) detect chemical biosignatures characterized by geochemistry, and (3) provide a detailed geochemical basis for a set of samples that are expected to be returned to Earth by a subsequent mission (Allwood et al., 2020). The Curiosity rover has found evidence of a habitable environment but has yet been able to detect paleo-life or evidence

of biosignatures in Gale Crater (Allwood et al., 2020; Grotzinger et al., 2014). An example of how PIXL could detect biosignatures would be to correlate sedimentary textures associated with the presence of microbial mats to the elemental distribution of the grains. With PIXL in Jezero crater, biosignatures will hopefully be detected with the unique μXRF technology.

This project geochemically characterized basaltic sediment in grain size fractions to examine physical and chemical changes in basaltic, volcaniclastic sediments transported through a glacio-fluvial-aeolian system. The specific objectives of this project were to (1) characterize basaltic sediment geochemically within different grain size fractions and through a glacial outwash field, (2) characterize a mineral-dominated field area versus a glass-dominated field area geochemically through a glacial outwash field, and (3) determine how μXRF can aid the interpretation and understanding of what is happening in the sand, silt, and clay sized fraction of a fluvial transect from source-to-sink.

Two hypotheses motivated this project: (1) Sediment will change geochemically with increasing distance from the source, and within differing grain sizes, due to the mixing of sediments from nearby volcanic input as well as the weathering alterations downstream. (2) Aeolian transported sediment will have a different geochemical and sedimentological signature and trend than fluvial transported sediment due to the mode of transport. This project refers to the 2019 and 2021 field locations as field areas. The proximal, medial and distal locations in each are referred to as field sites.

2. GEOLOGIC CONTEXT & FIELD AREA

Iceland sits atop a mantle hotspot and the divergent plate boundary of the North American Plate and Eurasian plate coincide (Pálmason & Sæmundsson, 1974). Due to the interaction between the Mid-Atlantic spreading ridge and the mantle plume, Iceland is a volcanically and tectonically active island made up of approximately 85% basaltic composition with the remainder consisting of more evolved igneous assemblages, such as rhyolite and a small percentage of intermediate rocks (Hawley, et al., 2017; Jakobsson, 1972; Jónasson, 2007; Gíslason, 2008). Iceland hosts diverse geologic features from this boundary such as tension fractures, normal faults, and volcanic fissures (Gudmundsson, 1994). The oldest Icelandic rocks date back to 15 Mya, around the middle-late Miocene, making the geology relatively young (McDougal et al., 1984).

Iceland's volcanic activity occurred during widespread glaciation and has resulted in glaciovolcanic eruptions throughout its geological history that create a distinct sequence of volcanic rocks and volcaniclastic sediments (Jakosson, 2008). Tuyas (or table mountains), tindars, and móberg sheets are all glaciovolcanic landforms and consist of pillow lava, cube-jointed (kubbaberg) lava, hyaloclastite tuff, and, in instances where the eruption reaches the top of the glacier, subaerial capping flows. Hot lava erupts under an ice sheet and melts the surrounding ice forming a melt pocket, which creates explosive activity. This interaction forms pillow basalts and kubbaberg basalt. Kubbaberg occurs due to rapid cooling creating its characteristic jointing (Smellie et al., 2008). As the eruption advances and the resulting volcanic landform starts to reach the height of the ice cap, an englacial lake is created. Overall, explosivity increases with height in a glaciovolcanic eruption as pressure from the overlying ice cap decreases as the volcanic landform reaches the top of the glacier, forming hyaloclastite tuff, which is a poorly sorted breccia of fractured pillow and kubbaberg units cemented by weakly altered ash. Once the volcanic landform

reaches the englacial lake stage, the ice cap is no longer suppressing the explosivity and a large Plinian or surtseyan ash column forms, such as during the famous 2010 eruption of Eyafjallajökull. Ash and lapilli in the ash column become well-sorted and can settle back down into the englacial lake, forming cross bedding and ripple stratification. Palagonite forms from the interaction of water trapped in the pore space of the tuff units with the hot ash and lapilli tuff matrix. Pillow and kubbaberg basalts are finely crystalline/aphanitic due to a rapid cooling environment. Tuffs can produce palagonite and clays due to the interaction with water, but generally they have abundant volcanic glass and X-ray amorphous materials due to the rapid quenching of the ash and lapilli (Bedford et al., 2022). Each of these morphologic textures can be recognized through morphology and mineralogy through the use of thin sections and/or XRF/XRD (Bedford et al., 2022). Currently, there are very few studies on how glaciovolcanism impacts the sedimentary record on Earth. By understanding the geologic source the sediment develops from, the better understanding of how the sediment physically and chemically changes with grain size and distance.

Within Iceland's postglacial basalts, three mineralogic groups exist: tholeiites, transitional alkali basalts, and alkali basalts (Jakobsson, 1972). Tholeiites are mafic extrusive rocks, usually associated with shallower melting. Alkali basalts are also mafic extrusive rocks yet associated with deeper melting. Typical mineralogy of Iceland includes olivine, plagioclase, pyroxenes, glassy material, and secondary minerals (Thorpe et al., 2019). Secondary minerals are mostly associated with finer fractions while rock forming minerals are associated with coarser fractions. Iceland's volcanic crust is dissected by glacial, fluvial, and aeolian processes. Sediments are then produced and transported (Arnalds et al., 2001).

Glacio-fluvial-aeolian outwash systems pervade the highlands of the island and the sediments derived from these systems are the target of this study. Glaciers, rivers, and aeolian

winds influence the geology of the island by eroding and chemically weathering the volcanic landscape and depositing sedimentary units during periods of volcanic quiescence (Arnalds et al., 2001). Glaciers are a main source of physical weathering of volcanic bedrock that produces a variety of sizes from gravel to silt derived from erosion (Arnalds et al., 2001). Glaciers tend to leave behind a large range of sediments when melting and give large amounts of sand to the environment (Arnalds et al., 2001). The second source of sand in Iceland is tephra (volcanic ash) and is mixed with glacial sands once transported (Arnalds et al., 2001). The dominant glaciers in our field areas are the Þórisjökull glacier and Kverkfjöll glacier, which is a tongue of the larger Vatnajökull glacier and feeds the Jökulsá á Fjöllum river system.

Fluvial systems draining the glaciers mobilize this sediment through catchments with rivers that range from a few km to over the main system, the Jökulsá á Fjöllum, which flows 206 km from the Kverkfjöll and Dyngjujokull glaciers to the north coast of Iceland, which was studied in this research. Fluvial systems are an important aspect of Iceland geology because they play a vital role in shaping the land and the transport of sediments. By weathering parent rocks and breaking down sand particles, rivers make-up the outwash systems of Iceland. Rivers not only physically change sediments, but chemically by sediment water interactions such as leaching and chemical weathering (Thorpe et al., 2019). Through the use of XRD and XRF, Icelandic environments upstream found more silicic material, like montmorillonite, whereas sediment downstream was more enriched in Fe-bearing phases, like ferrihydrite (focusing on clays; Thorpe et al., 2019). This observation leads to the theory that the upstream deposits record early states of alteration and more mobile cations (Mg, Ca, and Na) are leached to the solution, leaving the secondary products to become more clay rich. The downstream deposits are more enriched in Fe and immobile elements in a secondary product. Alternatively, the increased amount of altered material could be

transported further downstream due to the low density of the secondary products. This hypothesis suggests chemical alteration is a function of where the sample is taken in this project (Thorpe et al., 2019). The weathering and alteration of basaltic sediments in cold and wet environments, and the generation of a basaltic sedimentary record make it an ideal location to study the change of basaltic landscapes as an analog for Mars (Fairén, 2010; Wordsworth et al., 2015; Mangold et al., 2011).

The formation of the aeolian systems are intertwined with the glacial and fluvial systems. Aeolian systems form ripples and dunes, which were seen at both field areas in this project. Iceland hosts over 20,000 km of sandy deserts dominated by volcanic glass (Arnalds et al., 2001). This sand covers around 21% of the Icelandic surface (Arnalds et al., 2001). Previous studies have found that aeolian sands are typically well sorted and give an average of the rocks in the area of study, while fluvial sands are typically poorly sorted and display local source rocks and mineral sorting of pyroxene and feldspars (Bedford et al., 2022b). Aeolian sorting and transport are dependent on grain density, size and shape (Mangold et al., 2011). Aeolian processes lead to the fractional sorting of sediments relative to the source rock composition (Fedo et al., 2015).

Iceland has long been recognized as having rocks similar in chemistry and mineralogy to the martian crust and having sedimentary environments and a climate similar to the early Mars, which was thought to be cool and wet. The mineralogy of martian fluvial-lacustrine samples (collected from the Curiosity rover) are composed of plagioclase, felsic igneous minerals (alkali feldspar, tridymite, cristobalite, and trace amounts of quartz), mafic igneous minerals (olivine and pyroxene), phyllosilicates, sulfate minerals, phosphate fluorapatite, halite and X-ray amorphous materials (Rampe et al., 2020). These minerals are similar to those seen in Iceland. Mars, like Iceland, is thought to have ice-covered volcanoes associated with early Hesperian-aged, ridged

plains. These candidate glaciovolcanic landforms are thought to be characterized by the rough texture of the mounds and observed in the South polar region of Mars or flat-table mountains on the Martian surface (Ghatan & Head, 2002). Mars has a basaltic crust derived from paleo-volcanic activity and has evidence of abundant surface water that formed fluvial and deltaic systems during late Noachian to early Hesperian period (Catling, 2014). The sedimentary record suggests that Mars had both subaerial and subaqueous deposition (Malin & Edgett, 2000, 2003; Thorpe et al., 2021). Features on Mars include, but are not limited to, craters, dunes and ripples, volcanoes (e.g., Carr, 1976; Greeley et al., 2004; Sullivan et al., 2008; Fedo et al., 2015; Rampe et al., 2020). Features that indicate the presence of water include evidence of fluvial processes, lakes, and deltas (e.g., Milton, 1973; Sharp & Malin, 1975; Hynek et al., 2010; Thorpe et al., 2021). Although fluvial activity no longer exists on Mars, ice is present in the subsurface as well as the poles of Mars (Schorghofer and Aharonson, 2005). Mars, a basaltic-dominated world, has the potential to unlock mysteries of early solar system geology and habitable planets other than Earth (e.g., Mangold et al., 2011; Fedo et al., 2015; Mangold et al., 2015; Thorpe, 2018; Bedford et al., 2020; Rampe et al., 2020).

2.1 SAND-E Mars Analog Mission*

Sediment samples for this project were collected through a campaign-scale Mars-analog project, Semi-Autonomous Navigation for Detrital Environments (SAND-E). SAND-E used rover and drone techniques to investigate geochemical, mineralogical, and sedimentological changes along a source-to-sink transport pathway as part of a mission-style operation (Ewing et al., 2020).

*Modified with permission from Champion et al. "μXRF Investigation of Geochemical and Physical Grain Characteristics in a Glacio-Fluvial-Aeolian Catchment in Southwest Iceland." *53rd Lunar and Planetary Science Conference* (2022): Abstract #2409.

The science motivation of SAND-E is to characterize the physical and geochemical variability of basaltic sediments in a martian analog environment (Ewing et al., 2020). During this project, two separate field areas in Iceland were studied. The Þórisjökull sedimentary system in 2019 and 2021, the Jökulsa á fjollum sedimentary system (Fig. 1A). The areas were selected for the purpose of studying mineral vs. glass dominated basaltic environments. The Jökulsa á fjollum area is more glass dominated and the Þórisjökull area is near more mineral dominated environments (Baratoux et al., 2011; Mangold et al., 2011; Bedford et al., 2022).

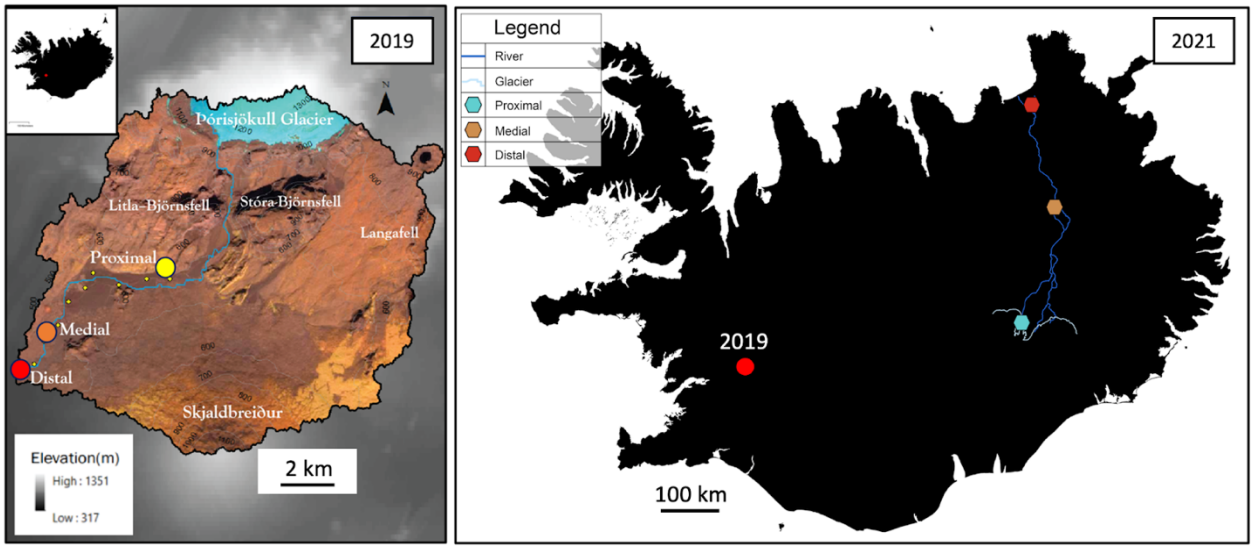

Figure 1. Field Area Maps. Maps display field areas from 2019 and 2021. (Left) A map of Iceland displaying the 2019 field area, a catchment of the small river, with proximal, medial and distal areas marked. This map includes the volcanoes and glaciers in the surrounding area (Modified with permission from Champion et al., 2022). (Right) The 2021 area is approximately 155 km in length (Kashauna and Stollis, pers. comm.).

2.2 Þórisjökull System Field Area (Summer 2019)

Þórisjökull volcanic field (Fig. 1, left) is within the Þórisjökull glacial outwash plain in southwest Iceland. The Þórisjökull volcanic plain is dominated by fluvial and aeolian sedimentary processes, with sediment originating from the volcanoes surrounding the area (Bedford et al., 2021). The four main volcanic sources in the field area include three tuya intraglacial volcanoes

(Þórisjökull, Lítla Björnsfell, and Stóra Björnsfell) and a shield volcano (Skjaldbreiður, Fig. 1B) (Bedford et al., 2022). Litla-Björnsfell was divided into upper and lower units based on changes in tuff morphology identified in the field (Bedford et al., 2022). Litla and Stóra Björnsfell both contain subaerial capping units, although Upper Litla Björnsfell represents a different eruptive period and overlies the Lower Litla Bjornsfell capping unit. The subglacial volcanic units present within each intraglacial volcano include pillow basalts, kubbaberg lava, and hyaloclastite tuff (Bedford et al., 2022). All morphologies present within the intraglacial volcanoes and interglacial volcanoes in the area are present within the sedimentary system, imparting different geochemical and mineralogical characteristics associated with each source. The main contributors to the sedimentary system at the proximal site are the kubbaberg, pillow and tuff morphologies of the intraglacial volcanoes (Fig. 1) (Bedford et al., 2022). With increasing distance along the sedimentary system, sediments derived from the more crystalline and feldspar-rich Skjaldbreiður source increase in abundance. Meanwhile, the altered palagonite from the intraglacial tuff units significantly decrease in abundance between the proximal and distal sites, likely a result of physical and chemical weathering partitioning the alteration products from the source into the finest grain size fraction for both fluvial and aeolian environments (Bedford et al., 2022). With multiple geologic sources of sediment, sediment mixing will have an impact on the geochemical makeup of sand through the transect and grain size fractions. This project will analyze the geochemistry of the sediment along the transport path and allow for the discovery of how the geochemistry changes with increasing distance from the source.

We sampled 3 field sites along the Þórisjökull sedimentary system (Fig. 1, left). The closest to the glacier was the proximal site (6.3 km from Þórisjökull glacier), the medial (11.3 from the glacier), and the farthest, distal (14.4 km from the glacier). The proximal site was positioned on

an alluvial fan at a transition in the glacial outwash stream to a shallower gradient. The sediment was poorly sorted and with multi-colored pebbles and cobbles, dark sand, and light-toned mud draping other sediments. Features such as aeolian ripples were present near the fluvial near. The medial site did not have an active fluvial channel but an abandoned channel was present. This site contained boulders where lava outcrops collapsed as well as aeolian ripples near outcrops. The distal site also had an inactive fluvial channel yet apparent fluvial deposits. The sand was finer and better sorted than the previous two sites. Large boulders as well as large aeolian and fluvial bedforms were apparent with light-toned silt found to drape over the large aeolian bedforms. Measured through XRD, primary igneous minerals in the source rocks at this field area include olivine, plagioclase feldspar, and pyroxenes (augite and diopside), and an X-ray amorphous material that was likely volcanic glass and palagonite (Bedford et al., 2022). Secondary alteration minerals are not abundant, but include hematite, gibbsite, and some poorly formed phyllosilicates (likely smectite) (Bedford et al., 2022). The primary igneous minerals and amorphous glass were also identified in the sediments, with no phyllosilicates detected and rare hematite (Rampe et al., 2019; Bedford et al., 2022b).

2.3 Jökulsá á Fjöllum System Field Area (Summer 2021)

All sites studied in 2021 occurred along the Jökulsá á Fjöllum river. Kverkfjöll, which feeds Jökulsá á Fjöllum, is an outlet glacier of the Vatnajokull glacier, and adjacent to the Kverknukhar volcanic system (Fig. 1, right). The Vatnajökull glacier is the largest glacier in Iceland measuring around 8,300 km (Stefánsdóttir and Gíslason, 2005). This field area is also SE of the Dyngjufjöll mountain range on the Odaðahraun lava field that includes the eponymous Askja volcano. Askja volcano was most active in the Pleistocene (Brown et al., 1991). This field area is another source-to-sink environment, like the Þórisjökull volcanic field. Jökulsá á Fjöllum is the

river system that flows from Vatnajökull and carries sediments from the glacier to the surrounding areas and throughout the transect. Sediments in this field tend to be more glass-dominated than the Þórisjökull volcanic field (Baratoux et al., 2011). These sands were derived from volcanic flows that occurred in the Holocene (younger than 11,000 years ago) and/or the Upper Pleistocene (11,000-800,000 years ago) (Baratoux et al., 2011).

The Jökulsá á Fjöllum catchment is larger, and the river (206 km) is longer than the Þórisjökull system giving rise to more fluvial and aeolian transport, sorting, and/or alteration. The difference in length of these two field areas adds a variety to this study as we can investigate how the length of a basaltic volcanic transect will affect the intensity at which sediment changes throughout a transect. Like Þórisjökull, there were 3 areas of study along the traverse. The proximal site is ~1 km from Kverkfjöll, the medial site, ~79 km from Kverkfjöll, and the distal, ~159 km from Kverkfjöll (Fig. 1, right). The proximal site has parallel volcanic pillow–hyaloclastite ridges and post-glacial subaerial lava flows (Karhunen, 1988; Jóhannesson and Saemundsson, 1989; Carrivick et al., 2004). The medial site in this traverse was slightly off from the main fluvial channel and dominated by aeolian processes. The distal site was on a terminal delta leading into the ocean and fluvially dominated. The final stop of the traverse has an increased amount of vegetation from the increased amount of water.

3. METHODS

3.1 Field Methods

A fluvial and an aeolian sample were collected from each of the proximal, medial, and distal sites from the Þórisjökull and Jökulsá á Fjöllum systems resulting in six aeolian and six fluvial samples and twelve samples overall. This project uses bulk samples for fluvial and surface samples for aeolian (with the exception of 2019 distal aeolian <63-125 μm which was a bulk sample, and proximal fluvial which was a surface sample). Samples collected as bulk samples were scooped from the top ~5 cm of the sampling location resulting in an integrated grain profile that captures both surface and subsurface grains. Samples collected as surface samples were scraped from the surface, a few mm, using a scoopula sampling tool. Bulk sample collection resulted in the collection of a greater volume of sample than surface sampling. The rationale for these approaches was that bulk sampling collected grains representative of the accumulated fluvial and aeolian processes whereas surface sampling collected grains reworked at the surface by the last active fluvial or aeolian process. Where specific geomorphic or sedimentologic structures were present at the surface, samples were taken with the context of the structure. For example, targeted samples were taken from ripple crests and troughs to capture differences in these features. After samples were collected in the field in Iceland, they were shipped to the Department of Geosciences at Texas A&M University for laboratory preparation and analysis.

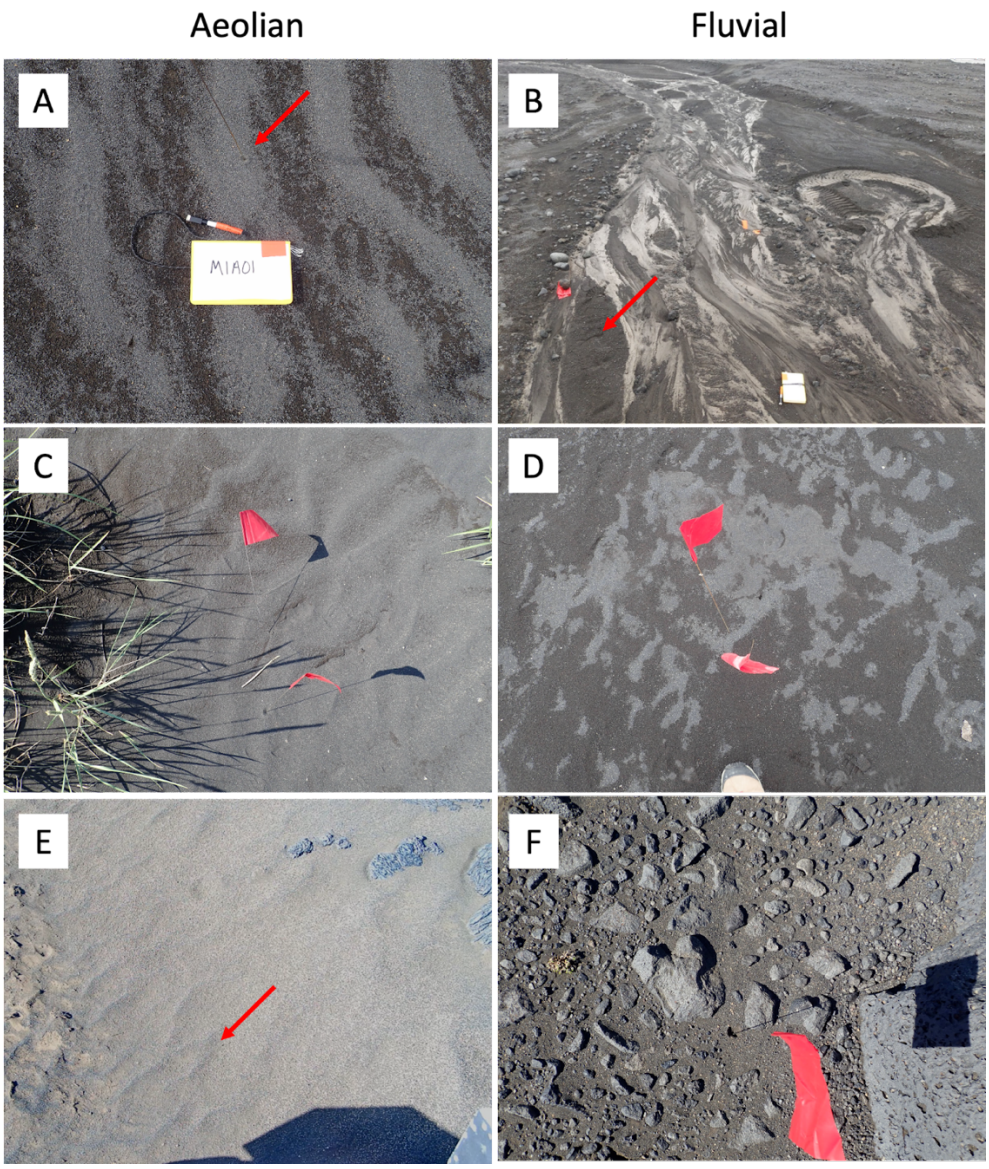

Figure 2. Sample Location Examples. Fluvial and aeolian sample locations for the 2019 and 2021 field areas. (A, B) 2019 medial site. (C, D) 2021 distal site. (E, F) 2021 medial site. Red arrows and flags point to specific sample collection locations. Field notebook is 4.75”x7.5”.

3.2 Laboratory Preparation Methods

The twelve samples were dried in an oven at 50 C to prevent any geochemical alteration from moisture. The oven was set to a low enough temperature to prevent any alteration from heat. Each sample was run through the Camsizer, an instrument that uses dynamic image analysis to measure grain size and shape. After using the Camsizer, each of the 12 samples was manually

sieved into 5 grain size separates to represent different Wentworth classes: 1 mm-710 µm (coarse sand), 710-250 µm (medium to coarse sand), 250-125 µm (fine sand), 125-63 µm (very fine sand), and <63 µm (silt and clay). These grain sizes fall into the category of sand (~63-2000 µm), silt/clay (<63 µm). The µXRF cannot analyze loose grain size larger than 1 mm due to the risk of damaging the instrument caused by the vacuum necessary for µXRF analysis. Therefore, grains above 1 mm were not analyzed for this project. Each separate is applied to double-sided tape and stuck to the plexiglass µXRF preparation plate (Fig. 3). Ti tape is applied at the corners of the samples in order to correlate to optical microscope images. The 2019 proximal aeolian <63 µm and 2021 proximal aeolian 710-1000 µm were not measured in this project due to the lack of material in the surface sample collected.

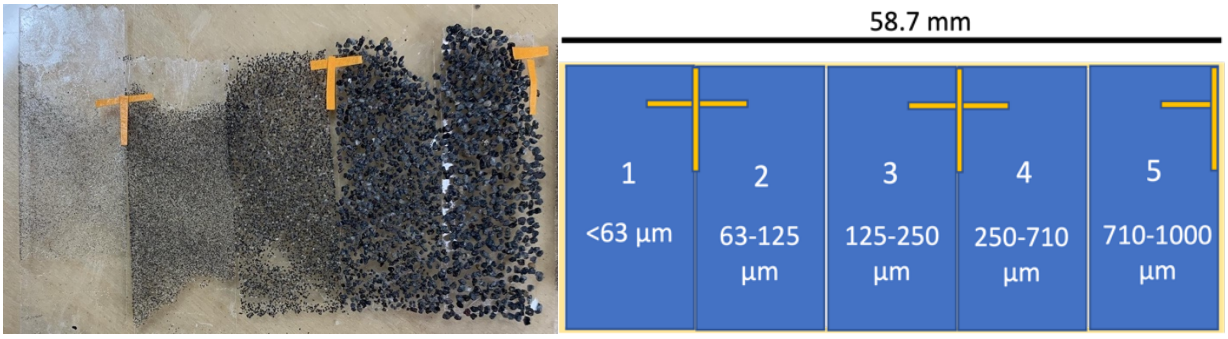

Figure 3. Plexiglass Layout of Samples. Ready for µXRF analysis. (Right) Sample layout of sieved grains on double sided tape and plexiglass. (Left) Schematic of sample layout with grain size fractions labeled. Orange tape is the Ti tape used for optical correlation (Champion et al., 2022).

3.3 µXRF and Geochemistry

µXRF measures a sample based on an element's energy or wavelength (Fig. 4). A primary X-ray source strikes an atom, and the X-ray is either absorbed or scattered through the material. The incoming photon interacts with a K shell electron and the electron is displaced to an unoccupied state and leaves a core hole called the photoelectric effect. A higher-level electron

takes the place that the previous electron left and emits a photon. An element can generate multiple X-ray lines due to the transfer of electrons between different orbitals to an inner electron shell of the atom.

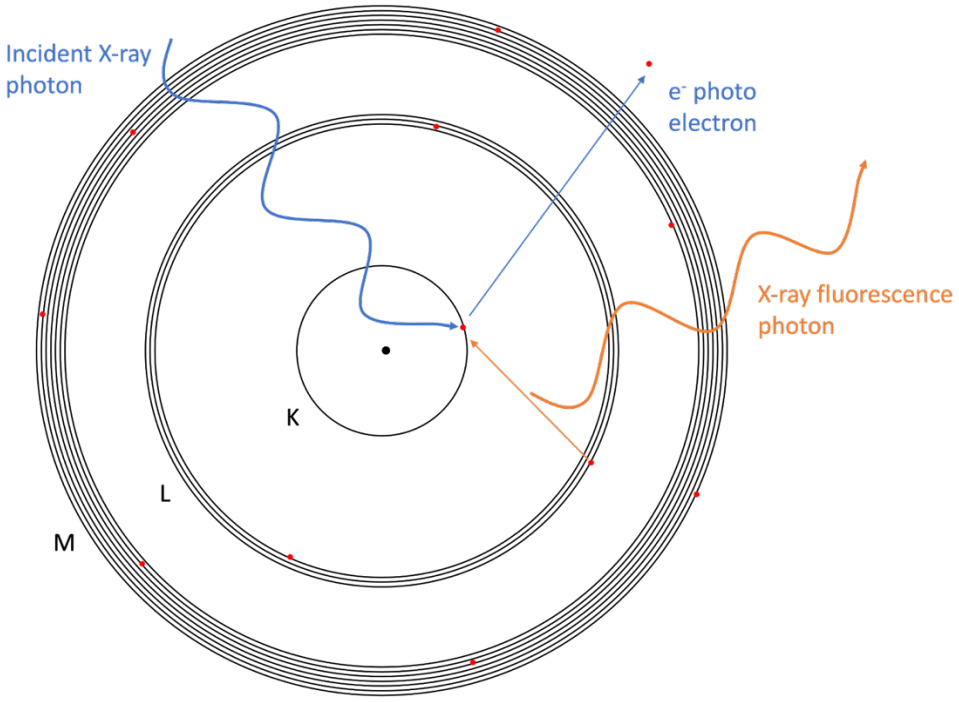

Figure 4. X-ray Fluorescence Diagram. Depicting incoming X-ray photon interacting with the deep core electron. The electron from a higher level takes the deep core electron's place and emits an X-ray fluorescence photon (modified from Basdevant & Rich, 2005).

The µXRF used for this project is the Bruker M4 Tornado Plus µXRF which consists of 2 x 60 mm energy dispersive silicon drift detectors at 45°, 4 ports for excitation and detection and a standard Rh-anode X-ray tube with polycapillary optic. The X-ray source consists of the emission of electrons from a cathode which accelerate onto the anode and cause the emitted radiation of the anode material. A 20 µm resolution was used to analyze 2 samples (a total of 10 individual grain sizes) at a time. I analyzed the 2019 samples and Dr. Mike Zawaski analyzed the 2021 samples. The total runtime for the 2 samples of an 11 by 2.3 cm area is approximately 14 hours (Fig. 3). With the 20 µm probe head, only one accumulation is necessary due to the high resolution being

acquired. A 100 µm probe head is most comparable to the PIXL instrument on NASA's *Perseverance* rover (Allwood et al., 2020). Each pixel provides unique elemental data based on the pseudo-intensity of the selected area. The brighter the pixel is of a corresponding element; the weight percentage of that element is greater in said pixel. This creates a detailed map of pixels with unique elemental data.

Error for µXRF quantification of elements is calculated by the µXRF instrument software as a basic counting error. This project reports error as absolute error in weight percent. The error is calculated as the reciprocal of the square root of the counts multiplied by the weight percent of an element detected and reported as absolute weight percentage (2 sigma). Counts for the µXRF is the number of detected X-ray photons. The more counts there are for an element, the lower the error will be. The formula used to calculate absolute error is:

$$Absolute\ Error\ in\ Weight\ \% = Weight\ \%\ of\ Elements\ \times \frac{1}{\sqrt{Counts}}$$

Another form of uncertainty in this project arises from analyzing loose sediment. With loose sediment applied to double sided tape, there is surface roughness or topography on each sample, which is different from measuring a polished core or hand sample. In the latter case, the µXRF is able to measure all points on the same plane, whereas for loose sediment, peaks and valleys within and between grains exist that create differentiation between amounts of an element from a high point to a low point. This error is greatest with the coarsest grain sizes due to large topography differences between the peak of the grain and the mounting plate. Finer and better sorted sediment were more uniform in height and closer to the mounting plate resulting in less

error related to this problem. Weight percentage would be different due to topography than if the sediment was powdered and homogenized.

Information depth is the depth in which the majority of μXRF signals come from. Information depth depends on the sample parameters, excitation conditions and fluorescence energy of the corresponding X-ray line. Due to the method chosen of applying sediment grain size fractions to double sided tape, each sediment sample has a different height. The topography difference of each sample affects the information depth. The heavier an element is, the information depth is increased. The heaviest element studied in this project is Fe with an information depth of 70 μm. The finest grain size fraction measured by the μXRF is <63 μm. With the information depth being greater than the finest grain size fraction, this will cause Fe to be underestimated. Mn is the next heaviest element with an information depth of 56 μm. With this, Mn should be quantified correctly as the information depth is less than the height of the grain size.

Data from element maps were quantified and reported as oxides using the *Bruker M4 Tornado Plus μXRF* software. Oxides were reported as normalized stoichiometric weight percentages. Oxides are used for weight percentage analysis because the major elements studied in this project are typically found bound to oxygen in their mineral constituents. By using oxides to analyze geochemistry there is less likelihood of an over or underestimate an element by using weight percent. The oxides studied in this project were NaO, MgO, AlO, SiO, KO, CaO, TiO, MnO, FeO. These oxides were chosen for this project because they are the major oxides that makeup basaltic environments. Major oxides are used because (1) they appear the strongest, with little background noise, as compared to harder to read minor elements in color maps, and (2) give an overview of the general composition changes with respect to grain size and distance from the source. FeO was chosen for the Fe oxide as opposed to Fe_2O_3 because Iceland's basalts are more

enriched in FeO phases. Elements, rather than oxides, are used for the element maps because this is the only option for the instrument.

3.4 Grain Characteristics Methodology

The grain roundness and texture of sediment was determined qualitatively by characterizing stereographic images by eye from a Zeiss Stemi 508 stereomicroscope (for the 2019 samples) and Dr. Nick Perez's Zeiss SteREO Discovery V.12 stereomicroscope (for the 2021 samples). Roundness was reported based on visual assessment of the grains using the Powers (1953) scale. Texture was qualitatively described as vesicular, and to what extent, or not vesicular (i.e., abundant, fine vesicles). Grain size of each sample was determined using dynamic image analysis. The sample funnels down a vibrating chute and then free falls in front of a white LED panel while high-resolution cameras capture grain properties (Fig. 5).

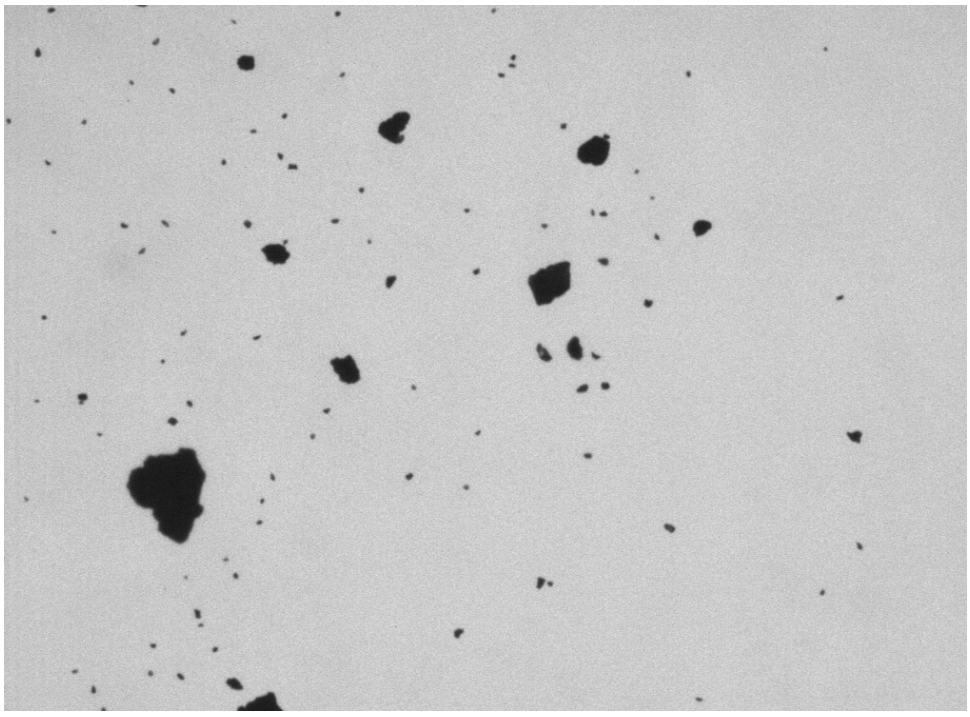

Figure 5. CAMSIZER Image. Grains falling in front of white LED panel. Grain size and shape are being analyzed. No scale bar is present or known for this image from the instrument.

3.5 Thin Section Methods

Thin sections were used to examine the mineralogy of individual grains. The thin sections were made from samples collected between the proximal and medial sites of the 2019 field campaign. The fluvial sample was collected 4 km from the proximal site at a river bar and an aeolian sample was collected 2 km from the proximal site from a ripple crest. A total of 6 thin sections were made from the <63, 125-250, and 250-710 μm grain size fractions of each of the aeolian and fluvial samples previously described. The embedded color was blue in order to distinguish the grains and intergranular pore space.

Point-counting method was used to count 300 grains in each grain size for an unbiased analysis of grain type. Six iterations of counting 50 grains were used to determine the accuracy of the measurements. Thin sections were analyzed and photographed under Dr. Nick Perez's Zeiss AxioScope A1 with transmitted light. Both cross polarized light (XPL) and plane polarized light (PPL) were used to determine the mineralogy and texture of the grains.

4. RESULTS

4.1 Grain Characteristics

Figure 6 shows the grain size distributions and sorting of the fluvial and aeolian samples from the 2019 and 2021 field areas. The fluvial samples from both field areas are coarser in the proximal and finer in the distal (Table 1 & Fig. 6B, D). The aeolian 2019 proximal are the coarsest and the medial are the finest. The aeolian 2021 distal are the coarsest and the medial are the finest. Overall, the fluvial and aeolian 2021 samples are finer than the 2019 samples with the 2021 aeolian samples being the finest of all the samples. The fluvial samples were less sorted than the aeolian samples, based on the slope of the cumulative distribution curve, where aeolian samples have a steeper curve, which represents a more uniform grain size. The 2019 and 2021 proximal fluvial are the least sorted of all the samples while the 2021 aeolian samples were the most sorted.

Tables 2 and 3 show that grain roundness varies with grain size, field area and site and distance along catchment from glacial outlet. The 2019 <63-250 μm fraction is angular to subrounded. The 2019 sites contain well rounded grains in the coarser grain sizes, beginning in 125-150 μm fraction (Figs. 7 & 8). The 2019 distal site has an abundance of rounded grains in this fraction, indicating that roundness increases with distance from the source. All grain size fractions in 2021 are angular to subangular, however the 250-1000 μm have a wider distribution of angular and rounded grains. The 2021 grains are overall more angular than the 2019 grains in most grain sizes. The environment of deposition as fluvial or aeolian did not affect the roundness of the sample.

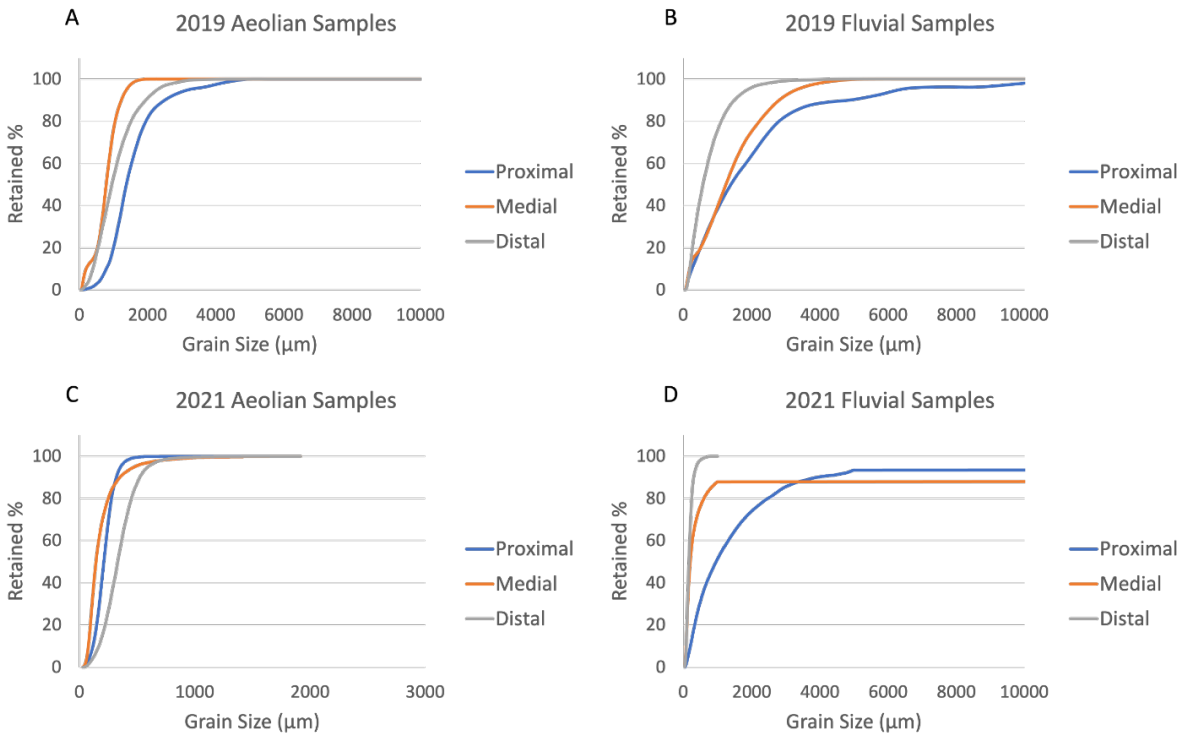

Figure 6. Grain Size Cumulative Frequency Plots. The 2019 (A & B) and 2021 (C & D) fluvial and aeolian grain size cumulative frequency plots. Blue is proximal, orange is medial, grey is distal. Note that the x-axis of the 2021 aeolian plot (C) has a smaller range than others. The 2021 medial fluvial had a loss of data above the 85% retained and therefore has a truncated distribution. Retained percentages associated with grain size fractions used in this project are reported in Tables 4 & 5.

Year	Sample	d10 (μm)	d50 (μm)	d90 (μm)
2019	Proximal Aeolian	785	1375	2501
	Proximal Fluvial	245	1388	4842
	Medial Aeolian	195	785	1230
	Medial Fluvial	173	1241	2801
	Distal Aeolian	531	1193	2184
	Distal Fluvial	189	569	1491
2021	Proximal Aeolian	117	212	320
	Proximal Fluvial	196	951	3886
	Medial Aeolian	78	144	352
	Medial Fluvial	78	198	1176
	Distal Aeolian	168	333	524
	Distal Fluvial	80	160	301

Table 1. Grain Size Distribution. Grain sizes of each sample determined by dynamic image analysis prior to sieving the samples for XRF.

Figures 7 and 8 show stereomicroscope photos of basaltic sediment from 2019 and 2021 samples in the respective grain size fractions of this project. The vesicularity of the basaltic sediment varies with grain size. The 250-1000 μm fraction possesses a vesicular texture while the <63-250 μm fraction have less frequent vesicles (Fig. 9). Visual assessment of the vesicles are smaller in the 2021 samples than in the 2019 samples, but there are no measurements to support this (Fig. 7F & 8F). Vesicles in the 2019 grains tended to be larger and less frequent than the vesicles in the 2021 samples. The vesicle interiors are typically coated in lighter-colored dust. The 2019 samples were coated to a greater degree of lighter material than the 2021 coarse grains.

Year	Sample	Grain Size (µm)	Grain Size Group	Grain Shape	% Retained	Type of Sample	Description
2019	Proximal Aeolian	<63	Silt & Clay	NA	0.0-0.1	NA	NA
		63-125	Very Fine Sand	anglular to subrounded	0.10-0.20	Surface	Lee side of ripple
		125-250	Fine Sand	anglular to subrounded	0.20-0.70	Surface	Lee side of ripple
		250-710	Med. to Coarse Sand	subangular to subrounded	0.70-9.0	Surface	Lee side of ripple
		710-1000	Coarse Sand	subangular to subrounded	9.0-20	Surface	Lee side of ripple
	Proximal Fluvial	<63	Silt & Clay	anglular to subrounded	0.0-0.6	Bulk	Coarse dark sand
		63-125	Very Fine Sand	angular to subrounded	0.60-4.2	Bulk	Coarse dark sand
		125-250	Fine Sand	angular to subangular	4.2-9.0	Bulk	Coarse dark sand
		250-710	Med. to Coarse Sand	angular to subrounded	9.0-28	Bulk	Coarse dark sand
		710-1000	Coarse Sand	subangular to subrounded	28-36	Bulk	Coarse dark sand
	Medial Aeolian	<63	Silt & Clay	angular to subangular	0.0-0.5	Surface	Ripple crest
		63-125	Very Fine Sand	angular to subrounuded	0.50-5.8	Surface	Ripple crest
		125-250	Fine Sand	angular to subrounuded	5.8-11	Surface	Ripple crest
		250-710	Med. to Coarse Sand	subangular to subrounded	11.0-40.0	Surface	Ripple crest
		710-1000	Coarse Sand	subangular to subrounded	40-80	Surface	Ripple crest
	Medial Fluvial	<63	Silt & Clay	anglular to subrounded	0.0-0.5	Bulk	Coarse grained sand
		63-125	Very Fine Sand	anglular to subrounded	0.50-5.4	Bulk	Coarse grained sand
		125-250	Fine Sand	anglular to subrounded	5.4-14	Bulk	Coarse grained sand
		250-710	Med. to Coarse Sand	subangular to subrounded	14-28	Bulk	Coarse grained sand
		710-1000	Coarse Sand	subangular to subrounded	28-40	Bulk	Coarse grained sand
	Distal Aeolian	<63	Silt & Clay	angular to subangular	0.0-0.1	Bulk	Ripple crest
		63-125	Very Fine Sand	angular to subrounded	0.1-0.6	Bulk	Ripple crest
		125-250	Fine Sand	angular to rounded	0.6-2.7	Surface	Ripple crest
		250-710	Med. to Coarse Sand	subangular to rounded	2.7-20	Surface	Ripple crest
		710-1000	Coarse Sand	subangular to rounded	20-35	Surface	Ripple crest
	Distal Fluvial	<63	Silt & Clay	angular to subangular	0.0-0.2	Bulk	Dark sand behind float
		63-125	Very Fine Sand	angular to subrounded	0.20-3.6	Bulk	Dark sand behind float
		125-250	Fine Sand	angular to rounded	3.6-19	Bulk	Dark sand behind float
		250-710	Med. to Coarse Sand	subangular to rounded	19-60	Bulk	Dark sand behind float
		710-1000	Coarse Sand	subangular to rounded	60-73	Bulk	Dark sand behind float

Table 2. 2019 Grain Characteristics. Shape information, approximate percentage retained of each grain size, the type of sample, and description of sample when in the field site.

Year	Sample	Grain Size (µm)	Grain Size Group	Grain Shape	% Retained	Type of Sample	Description
2021	Proximal Aeolian	<63	Silt & Clay	angular to sub-angular	0.0-1.7	Surface	Ripple crest
		63-125	Very Fine Sand	angular to sub-rounded	1.7-12	Surface	Ripple crest
		125-250	Fine Sand	angular to sub-rounded	12-69	Surface	Ripple crest
		250-710	Med. to Coarse Sand	angular to sub-rounded	69-100	Surface	Ripple crest
		710-1000	Coarse Sand	NA	100	NA	NA
	Proximal Fluvial	<63	Silt & Clay	angular to sub-angular	0.0-1.0	Surface	Coarse sediment
		63-125	Very Fine Sand	angular to sub-angular	1.0-4.8	Surface	Coarse sediment
		125-250	Fine Sand	angular to sub-angular	4.8-14	Surface	Coarse sediment
		250-710	Med. to Coarse Sand	angular to sub-rounded	14-42	Surface	Coarse sediment
		710-1000	Coarse Sand	very angular to sub-angular	42-52	Surface	Coarse sediment
	Medial Aeolian	<63	Silt & Clay	anglular to sub-rounded	0.0-4.2	Surface	Ripple crest
		63-125	Very Fine Sand	angular to sub-angular	4.2-40	Surface	Ripple crest
		125-250	Fine Sand	angular to sub-rounded	40-80	Surface	Ripple crest
		250-710	Med. to Coarse Sand	very angular to sub-rounded	80-98	Surface	Ripple crest
		710-1000	Coarse Sand	very angular to sub-angular	98-100	Surface	Ripple crest
	Medial Fluvial	<63	Silt & Clay	anglular to sub-rounded	0.0-5.0	Bulk	Coarse sediment
		63-125	Very Fine Sand	angular to sub-angular	5.0-29	Bulk	Coarse sediment
		125-250	Fine Sand	angular to sub-rounded	29-58	Bulk	Coarse sediment
		250-710	Med. to Coarse Sand	angular to sub-rounded	58-83	Bulk	Coarse sediment
		710-1000	Coarse Sand	sub-angular to sub-rounded	83-88	Bulk	Coarse sediment
	Distal Aeolian	<63	Silt & Clay	angular to sub-angular	0.0-0.6	Surface	Ripple crest
		63-125	Very Fine Sand	angular to sub-angular	0.6-5.1	Surface	Ripple crest
		125-250	Fine Sand	angular to sub-angular	5.1-27	Surface	Ripple crest
		250-710	Med. to Coarse Sand	anglular to sub-rounded	27-98	Surface	Ripple crest
		710-1000	Coarse Sand	very angular to subrounded	98-100	Surface	Ripple crest
	Distal Fluvial	<63	Silt & Clay	angular to sub-angular	0.0-4.0	Bulk	Sand behind float
		63-125	Very Fine Sand	angular to sub-angular	4.0-33	Bulk	Sand behind float
		125-250	Fine Sand	angular to sub-angular	33-82	Bulk	Sand behind float
		250-710	Med. to Coarse Sand	anglular to sub-rounded	82-100	Bulk	Sand behind float
		710-1000	Coarse Sand	anglular to rounded	100	Bulk	Sand behind float

Table 3. 2021 Grain Characteristics. Shape information, approximate percentage retained of each grain size, the type of sample, and description of sample when in the field site.

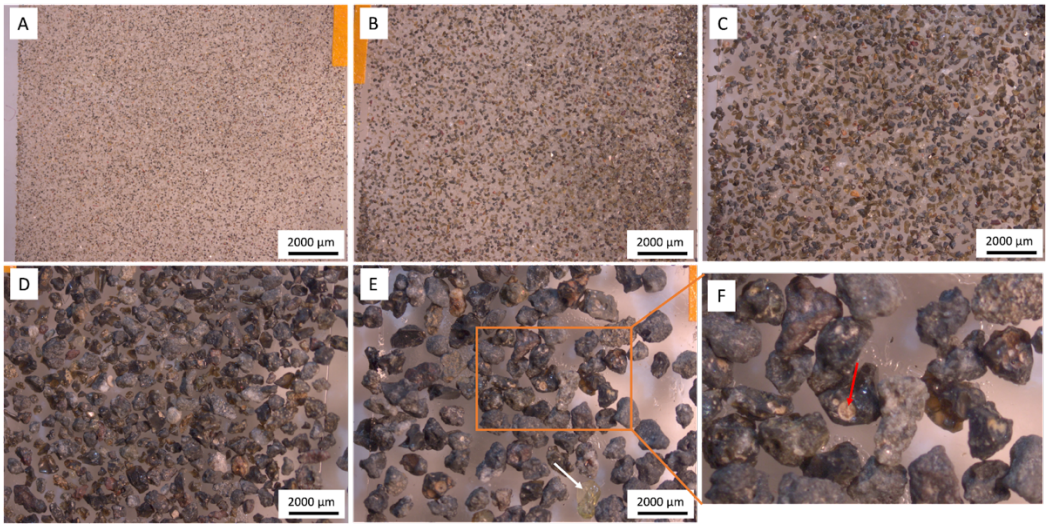

Figure 7. 2019 Grain Size Fraction Images. Five grain size fractions from the fluvial channel sands taken at Þórisjökull in 2019. (A) <63 µm, (B) 63-125 µm, (C) 125-250 µm, (D) 250-710 µm, (E) 710-1000 µm, and (F) zoom on the 710-1000 µm displaying vesicular texture. Images taken with a Zeiss Stemi 508 Stereomicroscope. White arrow in (E) showing a coarse olivine grain. Red arrow in (F) showing a coarse grain with a large vesicle filled with lighter material.

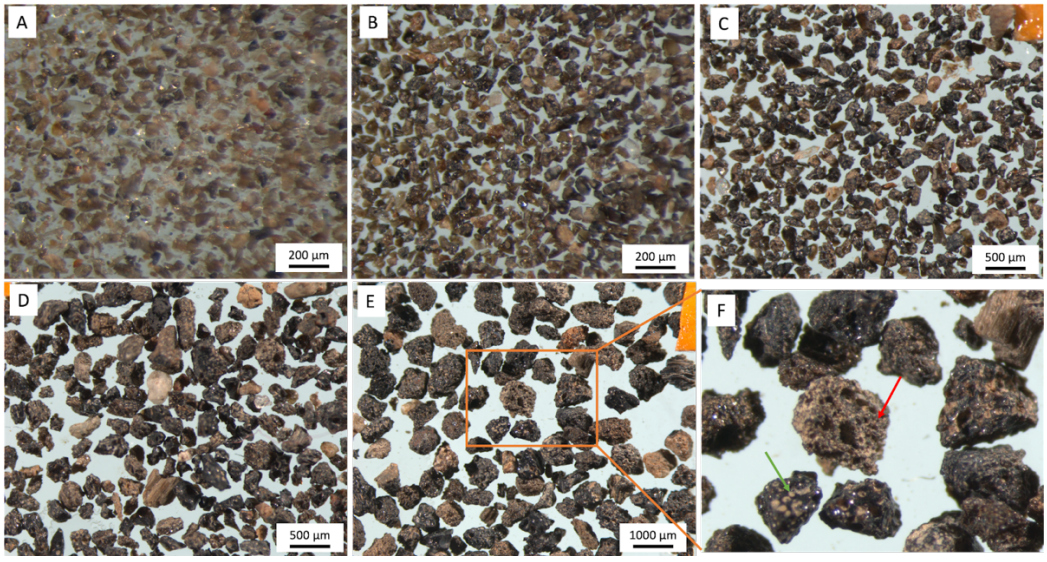

Figure 8. 2021 Grain Size Fraction Images. Five grain size fractions from the fluvial channel sands taken at Jökulsá á Fjöllum fluvial system in 2021. (A) <63 µm, (B) 63-125 µm, (C) 125-250 µm, (D) 250-710 µm, (E) 710-1000 µm, and (F) zoom on the 710-1000 µm displaying vesicular texture. Images taken with a SteREO Discovery V.12 Stereomicroscope. Red arrow in (F) points to many fine vesicles in a coarse grain near a larger vesicle. Green arrow in (F) points to fine vesicles filled with lighter material.

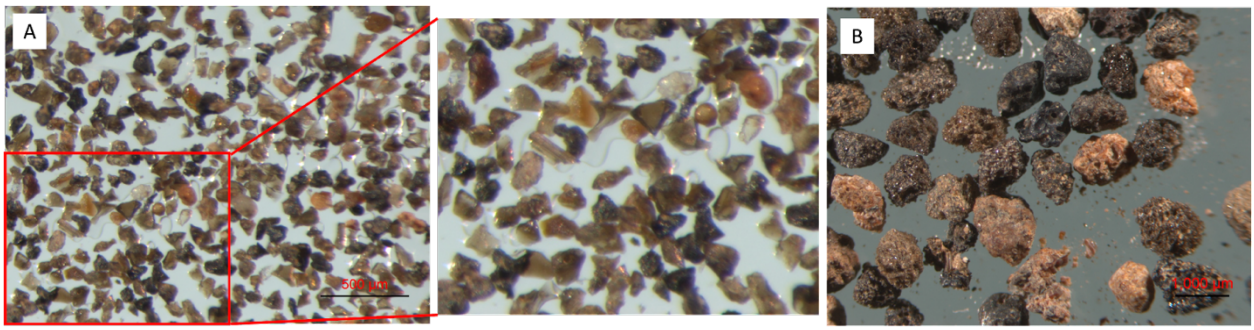

Figure 9. Aeolian Grain Vesicles Examples. Two aeolian grain size fractions from the medial 2021 site. (A) Grain size 63-125 µm with a limited number of vesicles in the grains. Zoomed in on the middle panel for detail. (B) Grain size 710-1000 µm with multiple vesicles within each grain.

4.2 Geochemical Oxide Analysis

Figure 6 shows the grain size distributions and sorting of the fluvial and aeolian samples from the 2019 and 2021 field areas. The fluvial samples from both field areas are coarser in the proximal and finer in the distal (Table 1 & Fig. 6B, D). The aeolian 2019 proximal are the coarsest and the medial are the finest. The aeolian 2021 distal are the coarsest and the medial are the finest. Overall, the fluvial and aeolian 2021 samples are finer than the 2019 samples with the 2021 aeolian samples being the finest of all the samples. The fluvial samples were less sorted than the aeolian samples, based on the slope of the cumulative distribution curve, where aeolian samples have a steeper curve, which represents a more uniform grain size. The 2019 and 2021 proximal fluvial are the least sorted of all the samples while the 2021 aeolian samples were the most sorted.

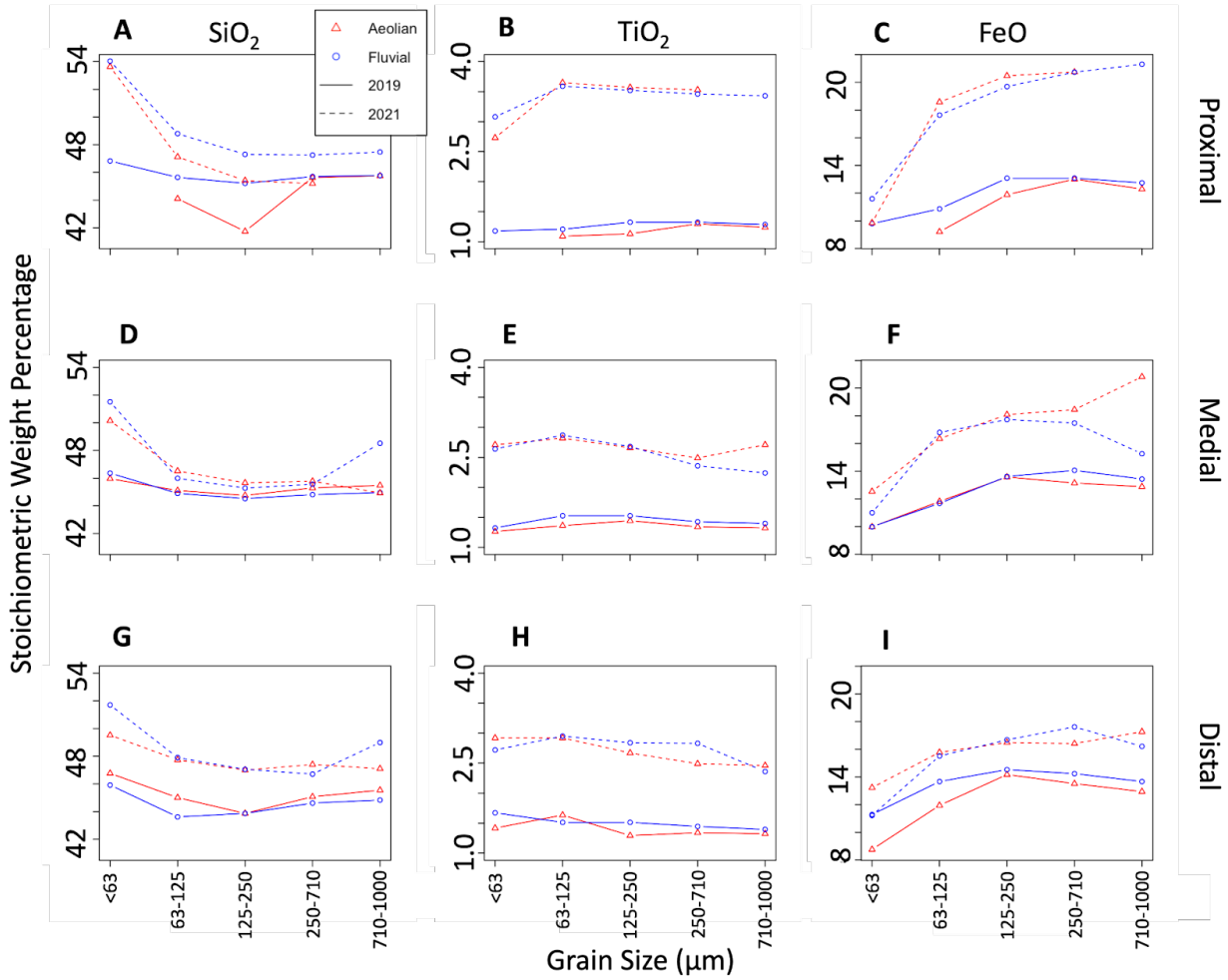

Figure 10. Stoichiometric Weight Percentages (SiO_2, TiO_2, FeO). 2019 & 2021 SiO_2 (A, D, G), TiO_2 (B, E, H), and FeO (C, F, I) through the grain size fractions and distance from the source. Lack of data in certain size fractions indicates that this size fraction was not present in the sample.

4.2.1 SiO_2

SiO_2 showed a large range in weight percent across grain size with only minor differences in location and among the 2019 and 2021 fluvial and aeolian samples. SiO_2 weight percent fraction decreases from a maximum in the <63 µm grain size fraction in all samples. A minima at the 125-250 µm grain size occurs in most samples (Fig. 10A, D, G). The greatest change occurs between the <63 µm fraction and the 125-250 µm fraction for all samples. At grain sizes greater than 250

μm, SiO_2 plateaus or slightly increases for all samples. The maximum weight percent SiO_2 occurred in the <63 μm 2021 proximal fluvial at 54.0% and the lowest weight percent occurred in the 125-250 μm fraction 2019 proximal aeolian at 46.8%.

SiO_2 slightly decreases with increasing distance from the source in each grain size fraction in the 2019 and 2021 fluvial samples. No clear trends from proximal to distal exist in the aeolian samples. Overall, the 2021 samples have higher weight percent SiO_2 than the 2019 samples. The 2021 samples possess a greater overall range with increasing grain size at 9.12% than the 2019 sample, which has a range of 5.08%. The trends and ranges are similar among the fluvial and aeolian samples across all years and locations with the only minor difference occurring with the 2019 proximal fluvial sample, which possesses more SiO_2 than the aeolian sample.

4.2.2 TiO_2

TiO_2 remains remarkably constant across grain size, locations, and environments (Fig. 10B, E, H). No significant trends emerge in TiO_2 concentration across grain size except in the transition from <63 μm to 125-250 μm fraction in the 2021 fluvial and aeolian proximal samples. Across all grain sizes, the proximal fluvial and aeolian 2021 samples are nearly two times as high in TiO_2 as in the medial and distal sites. No trend in TiO_2 concentration exists from proximal to distal in the 2019 samples. Overall, the weight percent TiO_2 is higher in the 2021 samples than in the 2019 samples.

4.2.3 FeO

FeO increases with increasing grain size across all grain sizes fractions in all years and locations (Fig. 10C, F, I). FeO sharply increases from 63 μm to 250 μm and plateaus or gently decreases or increases at larger size fractions. FeO decreases from proximal to distal in the 2021 samples except the <63 μm fraction which increases and drives an overall decrease in the range

toward the distal sites. The 2019 samples increase from proximal to distal. The fluvial and aeolian samples track similarly across grain sizes and locations with one significant divergence occurring in the coarsest fractions of the medial 2021 samples in which fluvial FeO decreases and aeolian FeO increases. The 2021 samples possess a higher overall weight percent of FeO than the 2019 samples.

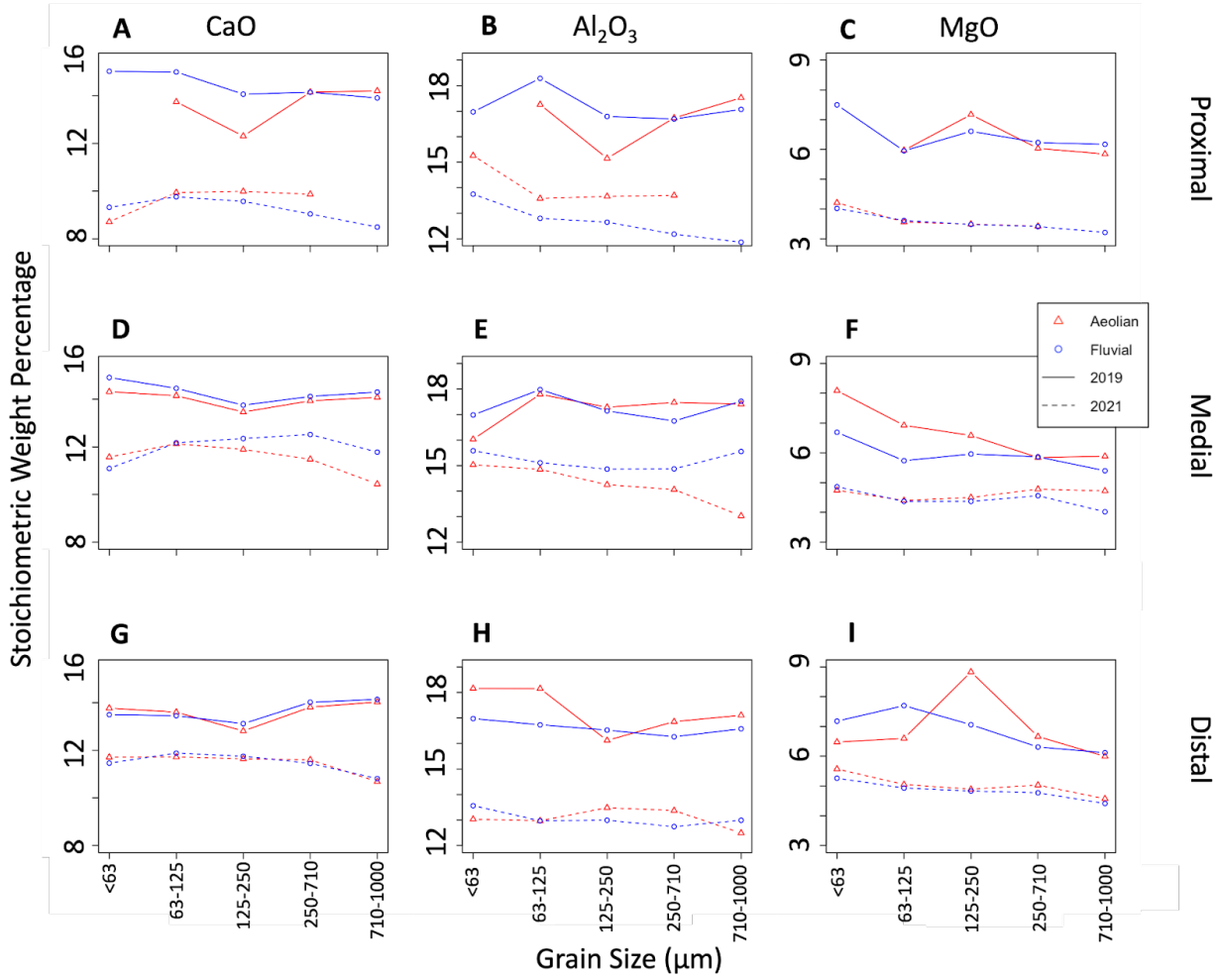

Figure 11. Stoichiometric Weight Percentages (CaO, Al_2O_3, MgO). 2019 & 2021 CaO (A, D, G), Al_2O_3 (B, E, H), and MgO (C, F, I) through the grain size fractions and distance from the source. Lack of data in certain size fractions indicates that this size fraction was not present in the sample.

4.2.4 CaO

Weight percent CaO in the 2019 field area, varies little with grain size, but has a consistent minima at the 125-250 μm size fraction (Fig. 11A, D, G). The 2019 125-250 μm fraction is depleted in CaO in the aeolian and fluvial samples at all locations. CaO in the 2021 samples decrease slightly with increasing grain size. The 2021 sediment increase in CaO from <63 μm to 63-250 μm and slightly decrease in CaO in the 250-1000 μm fraction. The 2021 CaO increases with increasing distance from the source while the 2019 samples typically decrease slightly with increasing distance from the source. The fluvial and aeolian samples contain similar weight percentages of CaO in all years and field sites. The 2019 field area has an overall higher weight percentage of CaO than the 2021 field area.

4.2.5 Al_2O_3

Although Al_2O_3 varies with grain size, no trend correlates those changes with grain size in the 2019 samples (Fig. 11B, E, H). The 2021 samples decrease in weight percentage with an increase in grain size except for the medial fluvial sample, which increases in the coarse fractions, and the 2021 distal site, which remains relatively constant with changing grain size. The 2021 fluvial Al_2O_3 increases from proximal to medial and decreases from medial to distal. The medial sample has the most Al_2O_3 of the sample sites. The 2019 field area has an overall higher weight percentage of Al_2O_3 than the 2021 field area.

4.2.6 MgO

Both 2019 and 2021 slightly decrease in weight percent MgO with increasing grain size in all sites (Fig. 11C, F, I). The 125-250 μm 2019 proximal and distal sites have an increase in the

aeolian samples. Both areas show an increase in MgO with increasing distance from the source in every grain size. Aeolian and fluvial samples are similar to each other across grain sizes, sites, and distance from the source. The 2019 field area has a higher weight percentage of MgO than the 2021 area.

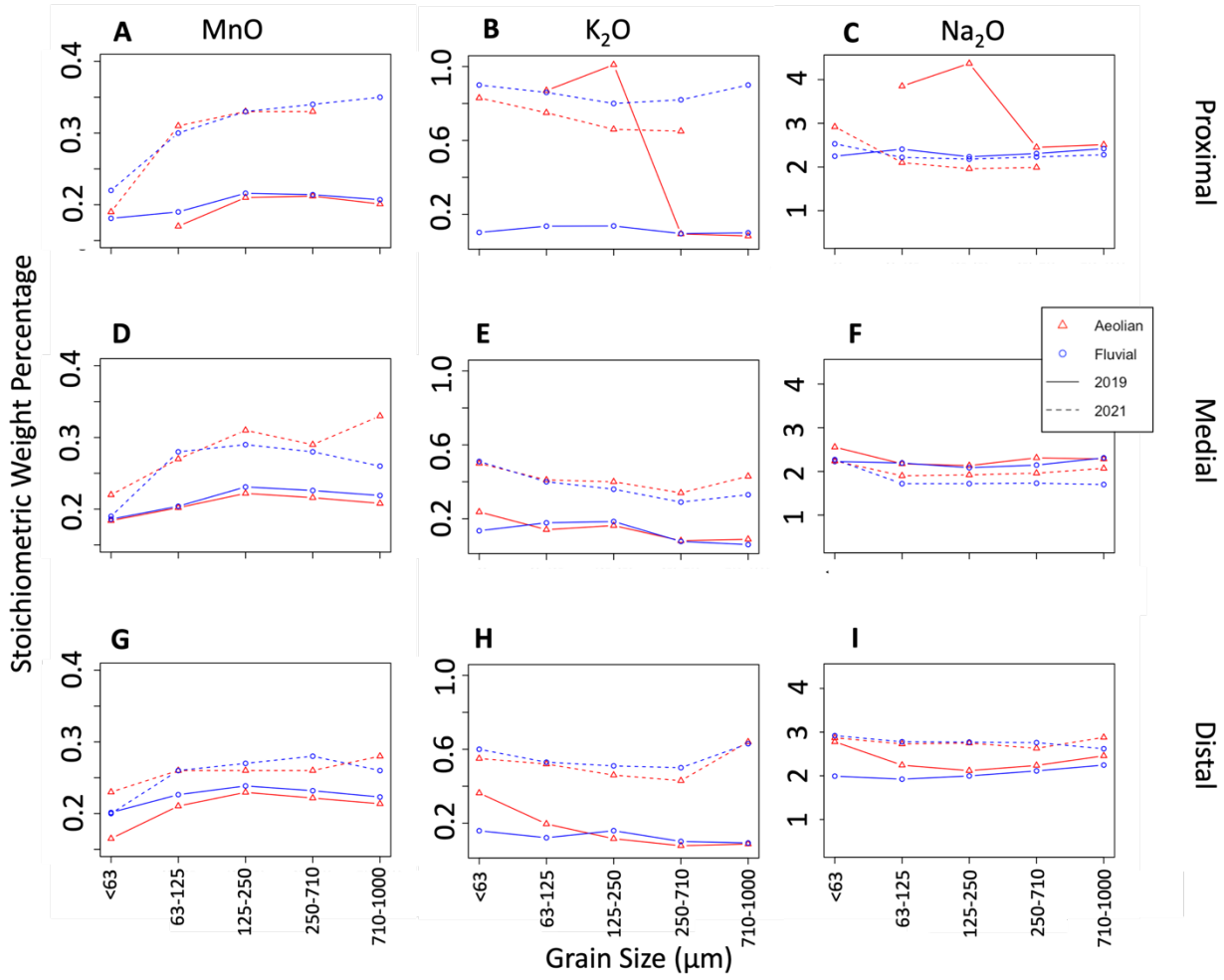

Figure 12. Stoichiometric Weight Percentages (MnO, K_2O, Na_2O). 2019 & 2021 MnO (A, D, G), K_2O (B, E, H), and Na_2O (C, F, I) through the grain size fractions and distance from the source. Lack of data in certain size fractions indicates that this size fraction was not present in the sample.

4.2.7 MnO

Weight percent MnO remains relatively constant across grain size, locations and transport medium (Fig. 12A, D, G). Both the 2019 and 2021 field areas show an overall increase in MnO

from <63-250 µm fractions and a decrease or plateau 250-1000 µm. The 2021 proximal and medial sites have an increase in grain sizes <63-250 µm compared to the remainder of the samples. The 2021 samples in each grain size decrease in MnO with increasing distance from the source and eventually are similar to 2019 weight percentages in the distal site. Overall, the 2021 area has a higher weight percentage of MnO than the 2019 area.

4.2.8 K_2O

Weight percent K_2O has a slight decrease with increasing grain size in all sites (Fig. 12B, E, H). The 2019 63-250 µm proximal aeolian sample has a higher weight percentage than the 2021 and an increased amount of K_2O than the other 2019 samples. In the 2021 samples, K_2O increases in the 710-1000 µm fraction. The 2019 sites remain constant in $K_2O$with increasing distance from the source. The 2021 area decreases in K_2O with increasing distance from the source. The 2021 area has an on average higher weight percentage than the 2019 area.

4.2.9 Na_2O

Weight percent Na_2O remains constant across grain size, locations, and environments (Fig. 12C, F, I) except for the 2019 63-250 µm fraction, which has a large increase in Na_2O by 2% more than the other sites and grain sizes. The 2019 aeolian sample possesses more NaO than the fluvial fraction. The 2021 proximal site has an increased amount of Na_2O followed by a decrease in the medial site and an increase in the distal site. The distal site possesses the most Na_2O in the transect. The 2019 proximal and medial sites are higher in Na_2O than the 2021 sites while the 2021 distal site is higher than 2019.

Year	Sample	Grain Size (μm)	Grain Size Group	SiO_2	TiO_2	Al_2O_3	FeO	MnO	MgO	CaO	Na_2O	K_2O
2019	Proximal Aeolian	<63	Silt & Clay	NA	NA	NA	NA	NA	NA	NA	NA	NA
		63-125	Very Fine Sand	44.100	1.090	17.260	9.210	0.170	5.970	13.750	3.850	0.870
		125-250	Fine Sand	41.740	1.130	15.150	11.890	0.210	7.170	12.310	4.370	1.010
		250-710	Med. to Coarse Sand	45.624	1.296	16.736	13.012	0.212	6.034	14.156	2.450	0.094
		710-1000	Coarse Sand	45.749	1.237	17.526	12.293	0.201	5.846	14.209	2.511	0.083
	Proximal Fluvial	<63	Silt & Clay	46.824	1.177	16.971	9.797	0.181	7.498	15.033	2.247	0.102
		63-125	Very Fine Sand	45.640	1.206	18.288	10.864	0.190	5.953	15.004	2.408	0.136
		125-250	Fine Sand	45.209	1.323	16.793	13.079	0.216	6.609	14.072	2.234	0.137
		250-710	Med. to Coarse Sand	45.700	1.323	16.693	13.081	0.214	6.230	14.156	2.308	0.096
		710-1000	Coarse Sand	45.775	1.284	17.071	12.745	0.207	6.172	13.913	2.420	0.100
	Medial Aeolian	<63	Silt & Clay	45.961	1.264	16.033	9.980	0.184	8.090	14.315	2.557	0.237
		63-125	Very Fine Sand	45.106	1.362	17.795	11.820	0.202	6.925	14.151	2.175	0.141
		125-250	Fine Sand	44.752	1.444	17.286	13.581	0.222	6.582	13.465	2.134	0.163
		250-710	Med. to Coarse Sand	45.294	1.342	17.474	13.146	0.216	5.840	13.934	2.311	0.081
		710-1000	Coarse Sand	45.475	1.322	17.409	12.882	0.208	5.885	14.081	2.285	0.089
	Medial Fluvial	<63	Silt & Clay	46.363	1.324	16.985	9.990	0.186	6.690	14.914	2.227	0.135
		63-125	Very Fine Sand	44.899	1.527	17.979	11.679	0.204	5.734	14.460	2.193	0.178
		125-250	Fine Sand	44.523	1.527	17.145	13.619	0.231	5.959	13.750	2.085	0.185
		250-710	Med. to Coarse Sand	44.811	1.427	16.750	14.065	0.226	5.864	14.119	2.145	0.077
		710-1000	Coarse Sand	44.956	1.398	17.522	13.436	0.219	5.398	14.301	2.311	0.060
	Distal Aeolian	<63	Silt & Clay	46.764	1.417	18.157	8.765	0.165	6.476	13.770	2.779	0.363
		63-125	Very Fine Sand	45.008	1.634	18.151	11.948	0.210	6.599	13.600	2.243	0.196
		125-250	Fine Sand	43.868	1.293	16.119	14.176	0.230	8.832	12.809	2.118	0.116
		250-710	Med. to Coarse Sand	45.074	1.340	16.856	13.520	0.222	6.662	13.809	2.238	0.078
		710-1000	Coarse Sand	45.546	1.323	17.105	12.945	0.214	5.994	14.025	2.458	0.087
	Distal Fluvial	<63	Silt & Clay	45.918	1.672	16.975	11.287	0.201	7.178	13.495	1.993	0.159
		63-125	Very Fine Sand	43.617	1.512	16.732	13.673	0.226	7.699	13.451	1.924	0.121
		125-250	Fine Sand	43.870	1.513	16.525	14.531	0.239	7.060	13.116	1.998	0.159
		250-710	Med. to Coarse Sand	44.615	1.445	16.262	14.242	0.232	6.309	14.017	2.113	0.101
		710-1000	Coarse Sand	44.833	1.395	16.576	13.671	0.223	6.119	14.134	2.246	0.093

Table 4. 2019 Stoichiometric Weight Percentages. Major oxides collected from quantified samples using the μXRF software.

Year	Sample	Grain Size (µm)	Grain Size Group	SiO_2	TiO_2	Al_2O_3	FeO	MnO	MgO	CaO	Na_2O	K_2O
2021	Proximal Aeolian	<63	Silt & Clay	53.63	2.73	15.26	9.86	0.19	4.21	8.71	2.92	0.83
		63-125	Very Fine Sand	47.12	3.65	13.58	18.58	0.31	3.56	9.94	2.10	0.75
		125-250	Fine Sand	45.41	3.57	13.66	20.48	0.33	3.49	9.99	1.96	0.66
		250-710	Med. to Coarse Sand	45.19	3.53	13.70	20.75	0.33	3.42	9.87	1.99	0.65
		710-1000	Coarse Sand	NA	NA	NA	NA	NA	NA	NA	NA	NA
	Proximal Fluvial	<63	Silt & Clay	54.04	3.08	13.75	11.59	0.22	4.02	9.32	2.53	0.90
		63-125	Very Fine Sand	48.80	3.59	12.80	17.64	0.30	3.61	9.76	2.22	0.86
		125-250	Fine Sand	47.30	3.52	12.65	19.70	0.33	3.48	9.57	2.18	0.80
		250-710	Med. to Coarse Sand	47.25	3.46	12.18	20.74	0.34	3.41	9.04	2.23	0.82
		710-1000	Coarse Sand	47.47	3.43	11.86	21.31	0.35	3.21	8.49	2.28	0.90
	Medial Aeolian	<63	Silt & Clay	50.15	2.71	15.03	12.54	0.22	4.74	11.57	2.24	0.50
		63-125	Very Fine Sand	46.52	2.82	14.85	16.35	0.27	4.40	12.13	1.90	0.41
		125-250	Fine Sand	45.66	2.66	14.25	18.09	0.31	4.50	11.89	1.92	0.40
		250-710	Med. to Coarse Sand	45.78	2.49	14.06	18.45	0.29	4.78	11.48	1.96	0.34
		710-1000	Coarse Sand	44.93	2.71	13.03	20.82	0.33	4.72	10.44	2.07	0.43
	Medial Fluvial	<63	Silt & Clay	51.52	2.64	15.58	11.00	0.19	4.86	11.09	2.27	0.51
		63-125	Very Fine Sand	45.99	2.87	15.11	16.80	0.28	4.37	12.17	1.72	0.40
		125-250	Fine Sand	45.28	2.68	14.86	17.73	0.29	4.37	12.35	1.72	0.36
		250-710	Med. to Coarse Sand	45.56	2.36	14.87	17.48	0.28	4.56	12.52	1.73	0.29
		710-1000	Coarse Sand	48.52	2.24	15.55	15.26	0.26	4.02	11.78	1.70	0.33
	Distal Aeolian	<63	Silt & Clay	49.52	2.92	13.03	13.23	0.23	5.57	11.71	2.87	0.55
		63-125	Very Fine Sand	47.74	2.92	12.97	15.78	0.26	5.05	11.72	2.73	0.52
		125-250	Fine Sand	47.00	2.67	13.48	16.49	0.26	4.89	11.64	2.75	0.46
		250-710	Med. to Coarse Sand	47.40	2.49	13.37	16.41	0.26	5.03	11.60	2.63	0.43
		710-1000	Coarse Sand	47.10	2.46	12.49	17.27	0.28	4.57	10.68	2.88	0.64
	Distal Fluvial	<63	Silt & Clay	51.70	2.72	13.56	11.22	0.20	5.26	11.46	2.92	0.60
		63-125	Very Fine Sand	47.90	2.95	12.97	15.52	0.26	4.93	11.88	2.78	0.53
		125-250	Fine Sand	47.05	2.84	12.99	16.68	0.27	4.83	11.75	2.77	0.51
		250-710	Med. to Coarse Sand	46.71	2.83	12.74	17.62	0.28	4.77	11.45	2.76	0.50
		710-1000	Coarse Sand	48.99	2.36	12.99	16.21	0.26	4.41	10.81	2.62	0.63

Table 5. 2021 Stoichiometric Weight Percentages. Major oxides collected from quantified samples using the µXRF software.

4.3 Element Maps

An element map is an image that shows the fluorescence of one element as pseudo-intensity or relative intensity. The value of each pixel in the map is the relative intensity of an element, which is an indicator of the relative abundance of that element in that pixel. Maps show individual elements (Fig. 13 & 14) or multiple elements (Fig. 15). Displaying multiple elements requires the images be stacked and assigned colors, typically red, green, and blue. Elements examined in this study using color maps include Al, Ca, Fe, Mg, Si, and Ti. Due to high noise in the images Mn, K, and Na were not examined. Noise arises due to the weight of the element and the low weight percentage detected. The low weight percent of Mn, K, and Na at less than 4.40% likely contributed to the high noise.

μXRF element maps typically have been used to investigate cores and hand samples in which the element data are contextualized by the position in the sample. Less common is the use of element maps to examine loose grains. Use cases are limited for benchtop XRF element mapping of loose sediment but one study used μXRF to conduct grain selection for geochronology (Storey et al., 2012). This μXRF, loose sediment project uses element maps of the sieved sand samples to examine grain scale variations in elemental distribution and assess the method for evaluating elemental data in unconsolidated sands. Visual inspection and qualitative assessment of the colors was the primary means of assessment of the maps. Only a few element maps are shown in this project as the element maps do not differ from site to site in a noticeable amount.

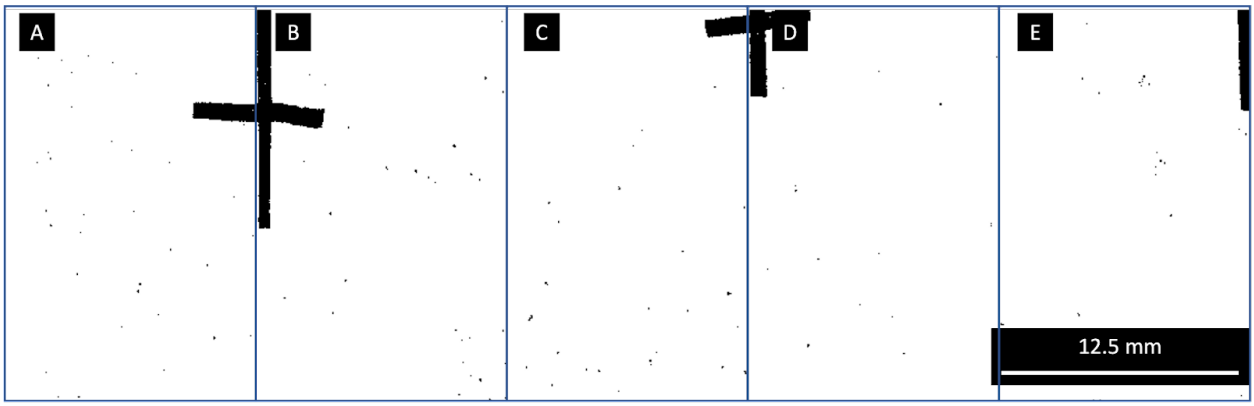

Figure 13. Ti Binary Element Map. Fluvial sample taken from the Þórisjökull area in 2019. Image displays Ti (A) <63 µm, (B) 63-125 µm, (C) 125-250 µm, (D) 250-710 µm, (E) 710-1000 µm. The black color displays where Ti is present.

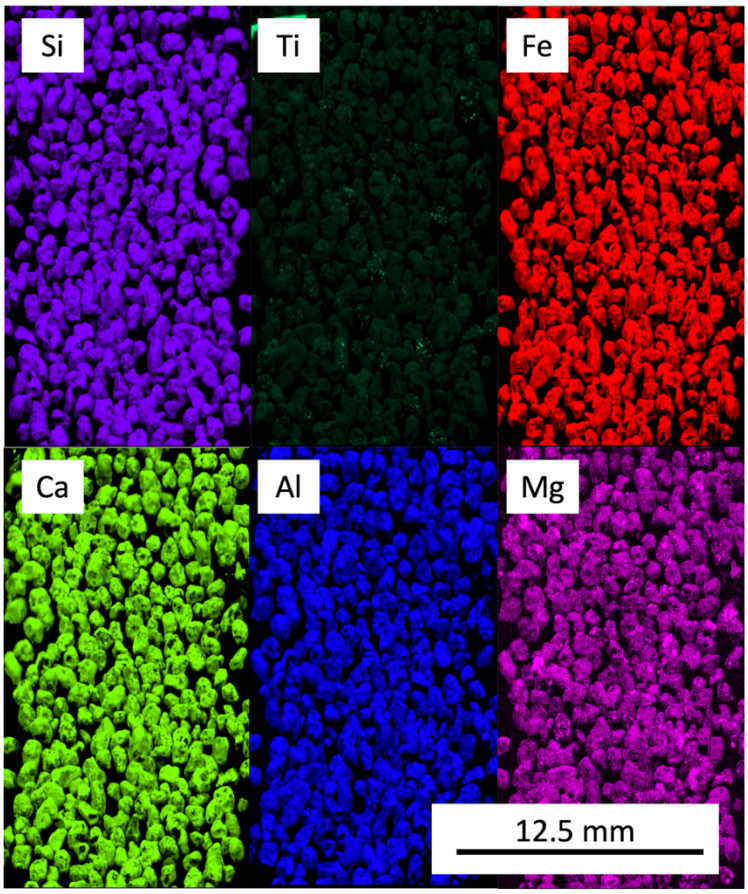

Figure 14. Single Element Maps. Si (purple), Ti (green), Fe (red), Ca (lime green), Al (blue), and Mg (magenta). Aeolian 710-1000 µm sample from the Þórisjökull area in 2019.

Fig. 13 shows the distribution of Ti across different size fractions. Ti is not represented by more than a few pixels in any of the grain sizes. For example, Ti appears in the same amount in the 710-1000 µm as it does in the <63 µm fraction. Ilmenite (FeTiO3) and titanomagnetite $Fe_2(Fe, Ti)O_4$ are two Fe oxides that most likely contain Ti in this environment. Collocation of Ti and Fe is common in all grain size fractions. It is displayed by an Fe, in red, and Ti, in green, map. The collocation of these elements are displayed by the color yellow in this map. If the Ti would have appeared green, the Ti would be present without Fe.

When looking at the fluorescence in single element color maps, Si, Fe, Mg, Al, and Ca appear to present in similar abundances throughout each grain size, transport distance, and sample setting (Fig. 14). To gain a sense of geochemical change through different variable studied, it is necessary to use stacked element color maps. To see change in geochemistry in a basaltic environment, a FeAlCa stacked color map proved to be the most useful in both field areas (Fig. 15). With Fe in red, Al in green, and Ca in blue, a general sense of basaltic mineralogy can be understood.

The 2019 FeAlCa color maps have little differentiation of geochemistry between grain sizes, transport mediums and field areas and are therefore not shown as a Fig. in this project. The hues of each element stay relatively the same with the exception of the <63-125 µm fraction. The <63 µm and 63-125 µm fractions of each 2019 field area appear cyan (Al and Ca), and the coarser fractions are more enriched in red (Fe). This does not automatically mean there is more Fe, there could just be less of other elements. The 2019 medial and distal fluvial coarser grains are more enriched in a deep magenta/purple indicating an enrichment in Ca and Fe. The 2019 distal aeolian <63 µm and 63-125 µm fractions appear greener than any of the other samples indicating an increase in Al.

The 2021 area has a greater differentiation in geochemistry between grain size fractions and field sites than the 2019 sites (Fig. 14). The 2021 proximal fluvial and aeolian <63 μm fraction have an enrichment in green (Al). The medial <63 μm has the same green enrichment, just not to the same extent as the proximal, and the distal is not enriched in green. The 2021 grain size fractions become increasingly red (Fe) with increasing grain size and distance from the source indicating an enrichment in Fe or a depletion in Al and Ca.

Examination of the coarser grains in the element maps revealed that each individual grain possessed more variation in geochemistry within a single particle than the finer sediments, which appeared to have little to no variation in geochemistry within a single grain. For example, Fig. 15 shows the coarser grains with multiple colors, which indicates multiple minerals exist within one grain. The resolution of the XRF limits firm evaluation of the presence of multi- or mono-mineralic grains in the fines fractions. The resolution of the μXRF scans was 20 μm and the finest grain size fraction was <63 μm. With this, the geochemistry of the <63 μm fraction would be displayed by 3 pixels of geochemical information per grain at most.

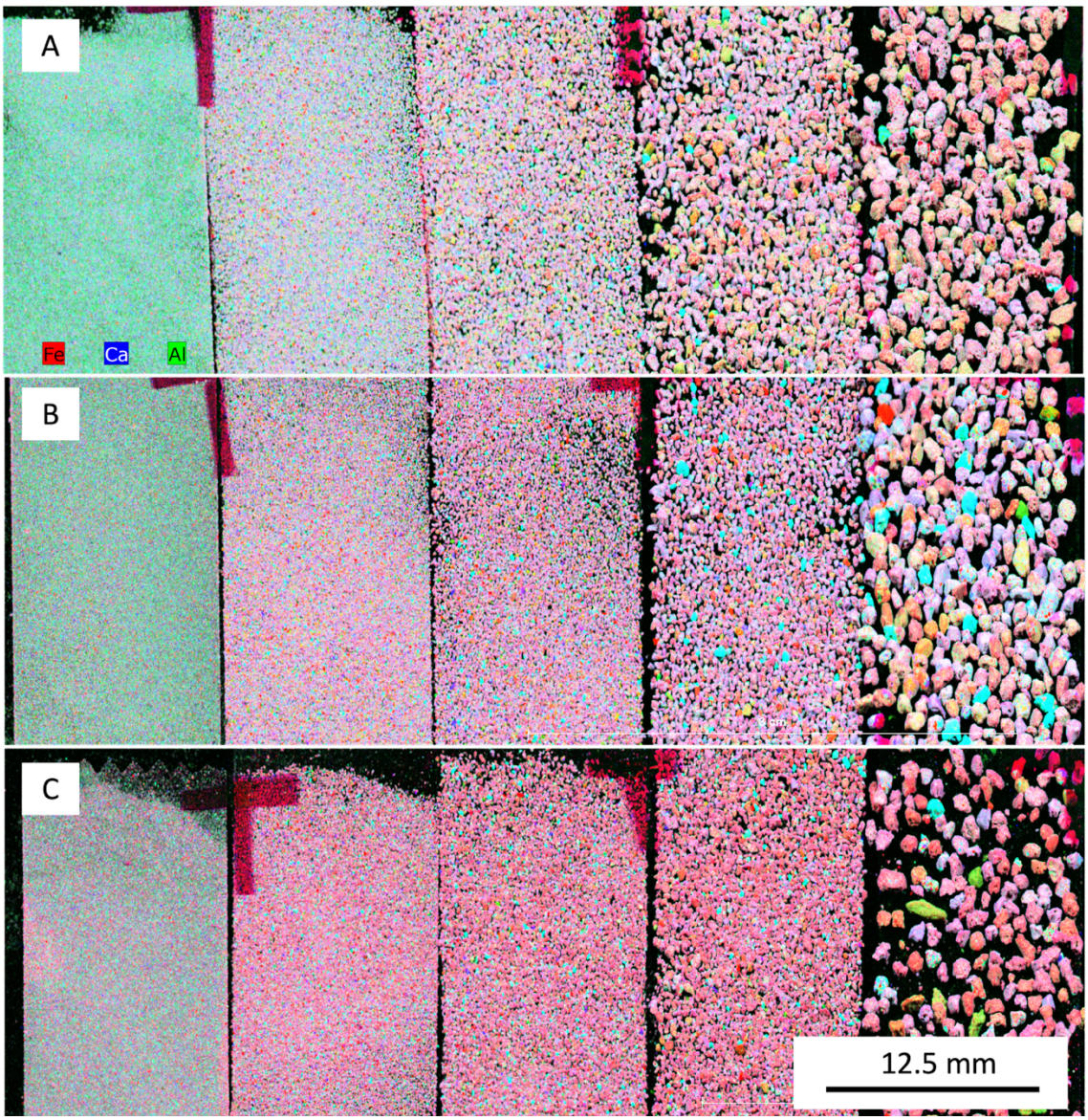

Figure 15. Stacked Element Maps. The color map of Fe (red), Al (blue), and Ca (green) 2021 fluvial samples where (A) is proximal, (B) is medial, and (C) is distal. The far-left grain size is <63 µm increasing in grain size to the far-right which is 710-1000 µm.

4.4 Thin Sections

Varied volcanic grain textures are seen within the thin sections of an aeolian and fluvial sediment sample (<63, 125-250, 250-710 µm) between the proximal and medial 2019 sites. The 250-710 µm grains (Fig. 16E & F) have groundmass textures with large and small phenocrysts. Glass grains exist with a vesicular texture and phenocrysts. Phenocrysts are typically olivine,

pyroxene, or plagioclase feldspar. Quench textures are displayed in multiple grains such as skeletal feldspar grains and plumose. Plumose is widely seen in 250-710 µm as a brown grain within both XPL and PPL with fan shaped, spherulitic patterns. Plumose is typically unmature pyroxene and plagioclase.

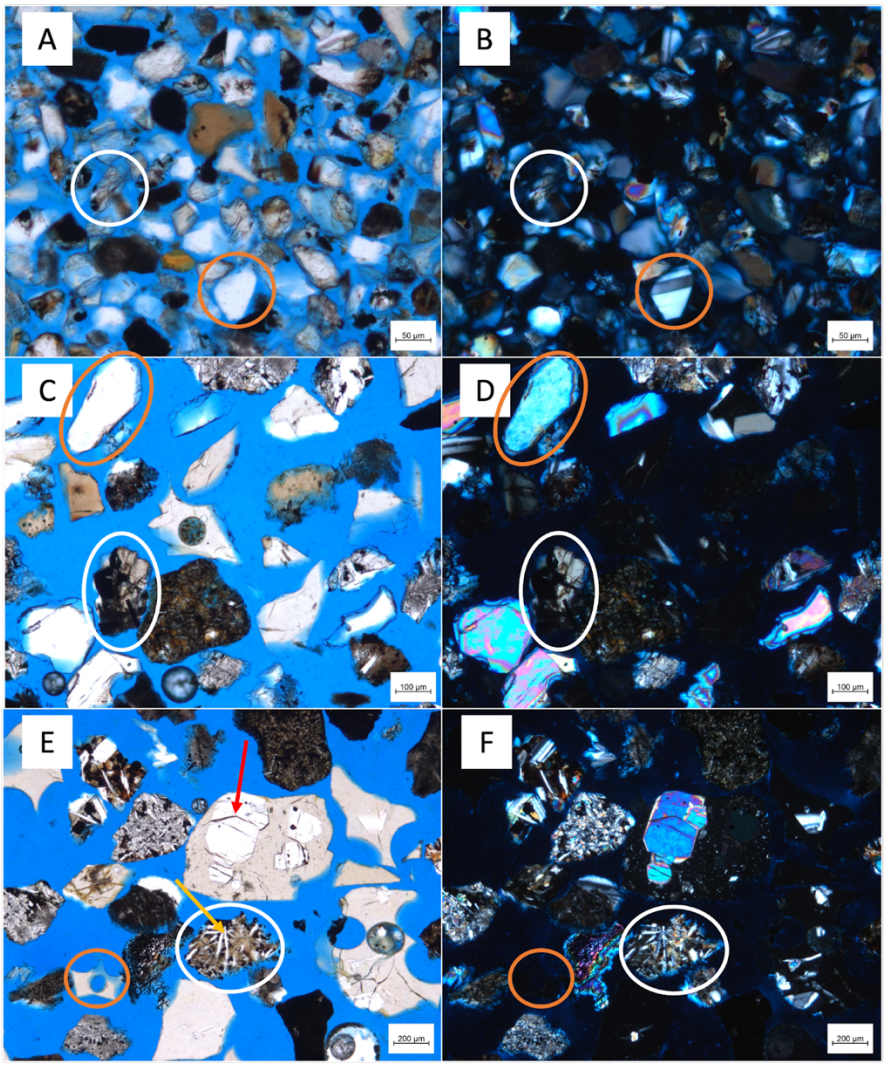

Figure 16. Petrographic Images of the 2019 Aeolian Sand. (A) <63 µm PPL. (B) <63 µm XPL. (C) 125-250 µm PPL. (D) 125-250 µm XPL (E) 250-710 µm PPL. (F) 250-710 µm XPL. The orange circles encompass monomineralic grains and the white circles encompass multimineralic grains. The red arrow in (E) points to an olivine phenocryst and the yellow arrow in (E) points to a skeletal feldspar. The scale for A & B is 50 µm, C & D is 100 µm, and E & F is 200 µm.

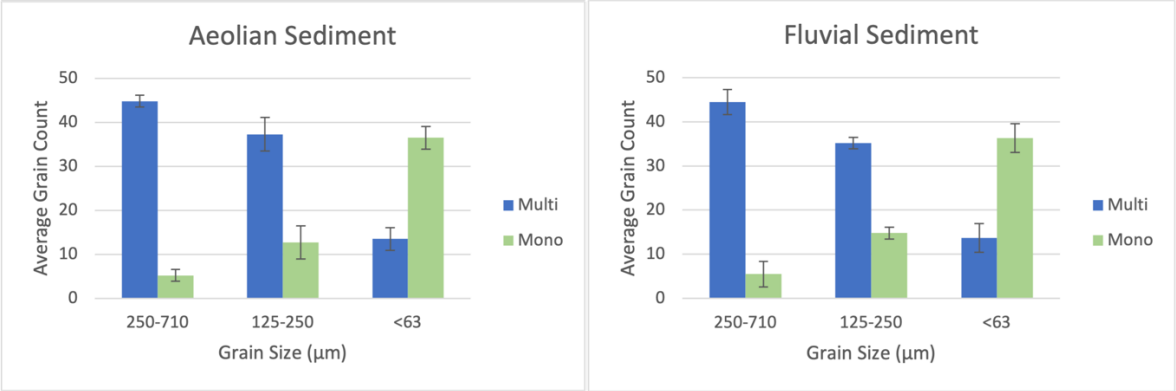

Figure 17. Bar Plots of Grain Counts. Aeolian sediment (left) and fluvial sediment (right). The average amount of multimineralic (blue) and monomineralic (green) grains there are in each grain size. Error bars are displayed on each thin section count and show standard deviation.

The 125-250 µm is very similar in the sum of textures to the 250-710 µm fraction. Groundmass textures and quench textures, such as plumose, are present in this grain size (Fig. 16C & D). Olivine appears as a monomineralic grain more often in this grain size than the 250-710 µm fraction.

The <63 µm fraction has a loss of groundmass texture and an increase in monomineralic grains (Fig. 16A & B). Grains are made up of glass, plagioclase feldspar, pyroxene, olivine and altered material that is difficult to determine mineralogy from thin sections alone. The finer grain size has a potential addition of quartz that was not seen in the coarser grain sizes.

The abundance of mono- and multimineralic grains was examined using thin section point counting analysis. Size fractions <710 µm were visually evaluated in the thin sections for the presence of one or more minerals comprising a single grain. Too few grains existed in the coarsest size fraction samples to acquire a statistically representative sample. The percentages reported are derived from the total amount of multi- or monomineralic grains counted over the total number of grains counted. Multimineralic grains comprised 89% of the 250-710 µm fraction of fluvial grains and 89.7% of aeolian. Additionally, multimineralic grains comprised 70.3% of the 125-250 µm

fraction of the fluvial grains and 74.7% of aeolian. Multimineralic grains comprised only 27.3% of the <63 μm fraction of the fluvial grains and 27.0% of aeolian (Fig. 17). This relationship shows a decreasing amount of multimineralic grains with a decrease in grain size. No difference exists in the amount of multimineralic versus monomineralic grains in the aeolian and fluvial samples. Error is reported as the standard deviation for the 6 iterations of point counting of 50 grains. The error for fluvial sediment was 2.88 for 250-710 μm, 1.33 for 125-250 μm, and 3.26 for <63 μm. The standard deviation for the aeolian sediment was 1.32 for 250-710 μm, 3.78 for 125-250 μm, and 2.59 for <63 μm.

5. DISCUSSION

Terrains dominated by basaltic volcanic material differ significantly from the quartzofeldspathic-dominated environments that make up most of Earth's landscape. General geological knowledge about the sedimentary rock cycle in which rock is eroded, weathered, transported, deposited, buried, and cemented derives from a quartzofeldspathic perspective. This perspective has presented challenges for understanding the sedimentary cycle on Mars, which possesses a basaltic crust, basaltic landscape, and basaltic sedimentary rocks. Iceland's varied basaltic volcanic terrains that are eroded and sculpted into glacial, fluvial, aeolian landscapes are Earth's best analog to early Mars in which basaltic volcanic were subject to a hydrologic cycle for thousands to millions of years. Deposits created from the erosion, weathering, and transport, of basaltic sediment on Mars are primary targets for exploration of past life, which creates a need to understand similar processes on Earth. Iceland's terrains afford a unique opportunity to study physical and geochemical changes of basaltic sediments subject to different sedimentary and cold-climate alteration processes.

5.1 Linking Particle Size and Geochemistry

5.1.1 Physical Sedimentology

Sedimentary processes have long been recognized to sort sediments based on the energy of the environment (Folk, 1974) and in this study, as expected, the fluvial sediments were overall coarser than the aeolian sediments. This is an expected outcome because the transport capacity of aeolian winds is less than that of fluvial. The fluvial samples are also less sorted than the aeolian, which is also expected given the greater transport capacity and larger fluctuations in energy in fluvial environments compared to aeolian environments. All samples possessed the same degree

of rounding indicating that the process did not greatly affect particle chipping and abrasion (Table 2 & 3). This is somewhat surprising given the significant differences in how sand is mobilized in fluvial and aeolian environments. Due to the fluid density and viscosity, collisions between sand grains in water are less energetic than in air and these differences typically contribute to greater angularity in fluvial sand and more roundness in aeolian sand. In quartzofeldspathic environments, aeolian sands are notorious for being among the most rounded particles across sedimentary environments. The similarity among roundness in the samples studied could be due to short transport distances in both the fluvial and aeolian systems. This would decrease the amount of time in transport and the probability of rounding grains. The similarity could also point to differences in how basaltic minerals round versus how quartzofeldspathic minerals round.

The 2019 and 2021 fluvial samples showed an expected grain size distribution with the proximal site having the coarsest sediment and sediment fining downstream toward the distal sites (Fig. 5B & D). This is to be expected as finer grains can be transported in almost all currents and therefore travel farther than coarser grains (Folk, 1974). As finer material is lighter, it can be more easily transported farther distances. The coarser grains tend to not be carried as far along the fluvial pathway as they may become too heavy for the transport medium. However, this generalization suggests that sediments are the same mass, which may not be the case with heavier mineralogies.

The two different field areas displayed differences in median grain size, vesicularity and roundness of the aeolian and fluvial sediments. Overall, the 2021 sediments were typically finer and more angular than the 2019 sediments. The 2021 aeolian sediments are the finest samples with most grains occurring within the less than 1000 μm size fraction (Fig. 5A & C). As the 2021 area is more enriched in glass, this result contrasts Cornwall et al. (2015) where mafic glass was slower to round and decrease in grain size. This difference could be due to the increased initial fluvial-

glacial weathering in the 2021 area. Additionally, a longer transport distance could influence size with fining of sediments further downstream due to increased exposure time to weathering.

The 2019 and 2021 <63-250 µm fraction have an angular to subangular or subrounded shape in grain sizes. The 2019 coarser grains tend to be subangular to subrounded/rounded, whereas the 2021 coarse grains tend to be very angular/angular while some grains are sub-rounded. This grain size & shape trend was observed in Goudie & Watson (1981) where angularity increases with decreasing grain size due to the lower impact energy released through collisions of grains (Tirsch et al., 2012). This study used quartz for experimentation, but due to the similarity of hardness of the basaltic minerals studied in this project, the results are comparable (Tirsch et al., 2012). The 2021 samples have less sorted sediment in the coarser fraction than the 2019, which suggests higher fluvial activity or less mature sediment.

2019 and 2021 grains display a vesicular texture in the coarser grain sizes but lack vesicularity in the fine fractions. Vesicular texture is caused by melt degassing at near-surface pressure (Polacci et al., 2008). It is assumed, by the results of this project, that as grains become finer, vesicularity is eroded away due to physical abrasion. The vesicles have the potential to be chipped away more easily due to greater surface area available for weathering. The 2021 grains have smaller, more abundant vesicles than the 2019 grains. The differences in the vesicularity are likely a consequence of how the source rock developed. Vesicularity is related to the depth of the eruption and composition of the magma. Typically, in subglacial eruptions, the closer to the surface has higher vesicularity and the lower portion has lower vesicularity (Moore, 1979). The greater degree of vesicularity in the 2021 sediment could be due to the lava flow being near to the surface which would indicate a higher cooling rate. The vesicles could also be due to the initial K content (Fig. 12B, E, H). The more K in a flow, the higher the initial HO content (Moore & Schilling,

1973). The 2021 area contained more K_2O in the flow, which could explain the increased vesicularity in the sediments.

5.1.2 Sedimentary Geochemistry

Results showed that the geochemistry of the samples was affected by grain size variations, distance from the source, mineral versus glass dominated source material, and differing transport lengths. However, differences in the geochemistry of sediments were not observed between fluvial and aeolian samples. As seen in Figs. 10-12, aeolian and fluvial sediment were very similar in weight percentages in every sample. This indicates that in this study, the physical sedimentary process did not have a strong effect on the geochemistry of basaltic sediments we sampled. It is likely that the aeolian sediment originated as fluvial sediments and that that fluvial system has reworked the aeolian system, which would have the effect of homogenizing the grain populations among these environments. As stated previously, the roundness of samples was also not affected by the transport medium. The mineralogy of the aeolian and fluvial sediments were similar which would also explain similar angularities. Again, this project hypothesized that aeolian and fluvial sediments will have differing geochemical and sedimentologic signatures. The geochemical and sedimentological observation here disprove a hypothesis of this project in which fluvial and aeolian sediments would show notably different geochemical signatures.

The samples from the 2019 and 2021 field areas displayed similar geochemical trends, yet some 2021 sediment trends increased or decreased by a greater range in comparison to 2019 (Fig. 10-12). SiO_2, FeO and MnO displayed the same trends in both field areas yet displayed a greater range in 2021. The 2021 sites had larger geochemical ranges in the proximal and lessened through the transect. This would indicate that the geochemical sorting of the sediment became more

homogenous with increasing distance from the source in the grain sizes, yet because the 2019 transect was shorter, this result was not seen.

The geochemistry of the samples from the 2021 medial site differed from the overall trend of the proximal and distal 2021 sites. CaO and Al_2O_3 had an increase in weight percentage in the medial where SiO_2, TiO_2, K_2O, Na_2O had a decrease in weight percentage in relation to the other sites along the transect. This change in geochemistry is most likely due to the medial site's lying on the terrace above the main fluvial channel of the Jokulsa a Fjollum. This site included a lava flow and an alluvial fan draining from nearby uplands. Sediments from the active Jokulsa channel likely had not recently affected the sediments at the medial site and they were more influenced by local outcrops resulting in a geochemical signal that differed from the other sites. An increase in AlO at the medial site could be a signal of the local source rocks, a greater degree of weathering due to the stability of the original source material, or longevity of exposure at the surface.

The 2021 sites had a greater range of weight percentages through the transect than the 2019 sites. MgO, Na_2O and K_2O are the only oxides to have a larger range in 2019 than 2021. The larger range of geochemical signatures indicates a more complex geology at the 2021 sites, which is to be expected as felsic material occurs through the transect (Furman et al., 1992). The increased geochemical range could also occur due to the longer transport distance allowing for more input from other source materials and chemical alteration. The large variation of TiO_2 in the 2021 sediment shows more diversity in volcanic rocks along the transect (Fig. 18).

Baratoux et al. (2011) discusses the diverse sands in Iceland where the Dyngjujökull field is glass dominated and sand fields near the Þórisjökull sand field are mineral dominated. Fig. 18 shows the 2021 sediments enriched in TiO_2 in comparison to the 2019 sediments enrichment in Al_2O_3, MgO, and CaO. Ti is an immobile element and indicative of more glass bearing phases and

a larger degree of partial melting. The 2021 samples possess more FeO, MnO and SiO_2 which is also indicative of more glass bearing phases. The enrichment of Al_2O_3, MgO, and CaO in 2019 sediments indicate more crystalline bearing rocks. Both areas have similar trends with increasing grain size (i.e., FeO increases with increasing grain size), however each area has differing trends with increasing distance from the source (i.e., FeO increases with increasing distance in 2019, yet decreases in 2021). This highlights the difference of mineral versus glass dominated fields and increased transport length allowing for higher degrees of alteration. This indicates that geochemical make-up and trends are more universal with grain size changes in basaltic environments, yet distance from the source trends are dependent on source material and length of transport.

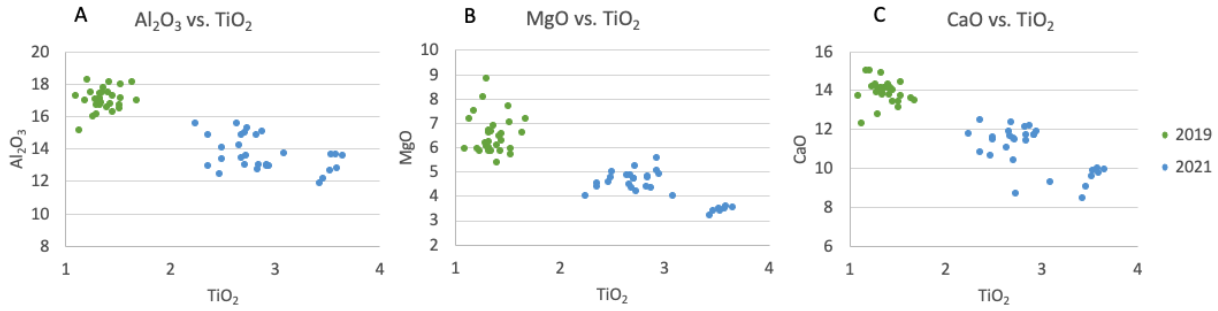

Figure 18. Comparison of Oxide Weight Percentages. All samples from 2019 (green) and 2021 (blue) typically found in mineral bearing phases and TiO, found in glass bearing phases. (A) Al_2O_3 vs. TiO_2, (B) MgO vs. TiO_2, (C) CaO vs. TiO_2.

The 2019 oxides in the <63-250 µm fraction have a greater range of weight percent oxides with increasing distance from the source, whereas the 250-1000 µm sediments have a decreased range of geochemical trend. This suggests that finer sediments have undergone more weathering or the source material in the 2019 sediment has a larger geochemical range when eroded into the fine fractions. This is typical for fine sediments due to increased surface area to volume ratios, and therefore have increased geochemical variation than the coarser sediments (Thorpe et al., 2018).

This also suggests that the majority of geochemical alteration happens in grain sizes <250 μm. The 2021 site does not follow this same trend with finer sediments, suggesting more diverse geologic source areas. There are more sources of sediment initially in the 2021 site as well as along the transport pathway. Increased transport length is thought to allow for more time to alter sediments geochemically and physically. This is surprising as basaltic glass is the most susceptible to weathering out of mafic rock-forming minerals and the grain size of this site was finer on average (Table 1; Nesbitt and Wilson, 1992).

MgO abundance can be related to presence of olivine in samples (Mangold et al., 2011). The 2019 sediment displayed a decrease in MgO with increasing grain size and an overall increase in MgO with increasing distance from the source (Fig. 11). The aeolian proximal and distal samples increased with respect to the other grain sizes in the 125-250 μm size fraction in proximal and distal. Mangold et al. (2011), relates variations in MgO to variations in olivine proportion in aeolian sediment. Olivine was seen to be enriched in 100-300 μm sands (in Mangold et al., 2011), an aeolian transportable grain size, in a mineral dominated environment (Mangold et al., 2011). This interpretation suggests that olivine in the 2019 area is enriched farther downstream and in finer grain sizes, especially in the 125-250 μm aeolian fraction. Thin sections showed an increase in olivine, especially in a monomineralic form, in the 125-250 μm grain size as well. This was not measured by point counting but was qualitatively observed. Similar to Bartoux et al., (2011) variations in the 125-250 μm of AlO-CaO are inversely related to MgO-FeO (FeO was used in this study). This suggests the olivine to plagioclase ratio is changing through grain size. SiO and FeO-MnO are also inversely related to one another. SiO_2 is enriched in finer grain sizes and FeO-MnO is enriched in coarser grain sizes. This suggests a higher degree of alteration in the finer grain sizes in the 2019 sediment.

In element maps, Ti never occurred beyond a few pixels in each grain size. This signals that the minerals carrying Ti, most likely ilmenite or titanomagnetite, appears isolated in small areas in the original crystallization. Weight percentages suggest the slight decrease in TiO_2 with increasing grain size, however, with the nominal change, this trend can be excluded as TiO_2 is an immobile element. More geochemical data would need to be analyzed to investigate the validity of this trend.

5.2 Application of µXRF to Loose Sediment

An objective of this project was to understand the limitations and benefits of µXRF when analyzing loose sediment. µXRF is a cheap and time efficient way to analyze geochemistry with limited preparation of samples, however, µXRF is typically used to analyze cores and hand samples (Flude et al., 2017). In this project, µXRF expanded the use of the instrumentation on loose sediment and allowed for the understanding of the geochemistry within grain boundaries otherwise impossible with XRF. This led to the investigation of thin sections and determined what grain sizes possess monomineralic grains. This indicates that µXRF can progress projects with additional information to ask further questions about samples otherwise difficult with common instrumentation. µXRF gives both visual data in the form of element maps, as well as stoichiometric weight percentages (Figs. 10-12). Both pair to support each other and enhance geochemical understanding of a sediment sample. Error in this study was extremely low due to the amount of counts collected for each sample (Appendix - Tables 6 & 7).

While µXRF can benefit the study of loose sediment, there are limitations to the use. µXRF is a relatively new way to study geochemistry, and a learning curve was necessary. As loose grains are not typically studied with µXRF, new methodology was developed in this project. µXRF allows for weight percentages and element map information acquisition, however, for element map

data, the results are relative to the scan itself. Therefore, element maps are not comparable to other maps outside the scan in which the map was created in this project, however may not be true universally. Additionally, the primary X-ray source of the μXRF analyzes the samples at an angle causing a stretch in the element maps which is exaggerated due the topography of larger grains. Due to the grain size studied in this project, the stretch of the color maps makes it difficult to analyze and compare shape and true color in stereographic images of coarse grains and impossible in the fine grains.

Due to the mixing of sources and homogeneity of the basaltic sediment, it is difficult to determine any notable trends in color maps of the samples that weight percentages did not indicate more clearly (Figs. 10-12). Many of the element maps look similar across grain sizes and transport distances when stacking a single or double element (Fig. 13-14). However, this gives assurance to an accurate result as the geology of the area has many minerals that make-up basaltic rocks and contain similar elements. Lighter elements were difficult to detect in element maps as they typically need a polished surface, where our samples were not (Flude et al., 2017). Although using color maps for basaltic environment analysis is not as useful as weight percentages, element maps would give more information in a mixed geologic environment (i.e., quartzofeldspathic and basalt). In these cases, the geology would be different enough from grain to grain to produce notable geochemical signatures indicative of the source. In basaltic environments, for this project, element maps are most useful as a solidifying geochemical visual analysis factor.

5.2.1 Monomineralic versus Multimineralic

Through the use of μXRF, geochemical analysis within grain boundaries led to the implementation of thin sections in this project to investigate volcanic mineralogy and texture in 2019 sediment. Understanding multimineralic and monomineralic grains are important as they aid

in the interpretation of the petrogenetic significance of crystallizing assemblages on Earth and Mars. However, there are limitations to understanding source material when using sand as the method of study (Boggs, 1968). Using the correct sediment grain size to understand a petrogenic environment is important as the grain size chosen can give different answers. Boggs (1968) discusses that the texture of the parent rocks are usually seen better in coarser grains rather than smaller grains. This project found a similar result in which coarser grains contain more multimineralic textures than finer grains (Fig. 17). Coarser grains are more likely to be less weathered than fine material, and hence, more reflective of the source rock and therefore are more likely to directly display textures from the source rock in this area. Volcanic flows host a variety of textures such as holocrystalline, hypohyaline, and holohyaline. These textures were observed in the 125-710 μm fraction through thin sections and classified as multimineralic. The <63 μm fraction lacks this texture. This suggests the groundmass texture is eroded away and broken into smaller monomineralic components, geochemically altered, or is transported further downstream. An alternative suggestion to the differing texture and mineralogy of the <63 μm grain size fraction could be from input of dust from other continents (Varga et al., 2021). Textures in the coarse grains include plumose with spherulite and bow tie quench texture and skeletal feldspar which indicate a high degree of cooling. The plumose texture is indicative of pillow basalts.

Sand is created from the physical weathering of rocks. Multimineralic grains can break into monomineralic grains due to collision during transport. Cornwall et al. (2015) discusses that grains become rounder through initial rounding and chipping of jagged edges which may occur along cleavage planes of weakness. These smaller fragments in turn are more likely to be monomineralic. The monomineralic grains in the coarse grain size fractions are phenocrysts from the melt. Likewise, the monomineralic grains in the fine grain size fractions are either fragments from a

larger phenocryst, altered material, or broken off minerals from the coarser grains or groundmass. The finer grain sizes have more monomineralic grains due to grains either breaking along grain boundaries into monomineralic components from a larger grain or are entirely altered into a secondary weathering product (Thorpe et al., 2019). Mafic glass is the most susceptible to chemical weathering, then olivine, plagioclase, clinopyroxene, and Fe-Ti oxide the least susceptible (Nesbitt and Wilson, 1992). Each primary mineral that makes up the basalt in our field areas weathers: Plagioclase weathers into kaolinite and Fe-smectite, olivine into iddingsite, Fe-smectite and ferruginous material. Pyroxene weathers into secondary amorphous and Fe-montmorillonite and primary glass into palagonite and Fe/Mg-smectite (Delvigne, 1979; Nahon and Colin, 1982; Crovisier et al., 1992, Pokrovsky et al., 2005; Vingiani et al., 2010; Thorpe, 2018). The finer grain sizes are more susceptible to weathering as they have a larger surface area to weather than coarser grains (Thorpe, et al., 2021).

5.3 Implications for Mars

Iceland, having similar geochemical and mineralogic geology as Mars, allows for an excellent analog for late Noachian to early Hesperian martian time period and geologic setting when water was once present. The humidity of Iceland leads to higher alteration than what is seen on Mars today. While the humid climate of Iceland is not analogous to present-day Mars, this study's findings could be relatable to a paleo-Mars environment. Mars Perseverance Rover, located in Jezero Crater, a 3.5-billion-year-old delta, contains multiple high-resolution instruments (i.e., PIXL & SHERLOC) to understand martian geology in a more holistic way (Schon et al., 2012; Goudge et al., 2015; 2017; 2018; Horgan et al., 2020; Mandon et al., 2020; Stack et al., 2020; Mangold et al., 2020; 2021; Farley et al., in review; Hollis et al., 2022). PIXL, in combination with other high-resolution instruments, allows for greater evidence of geochemistry

and mineral phases present. PIXL aims to characterize geochemistry in a spatial way to help reconstruct martian history and detect potential biosignatures (Allwood et al., 2020). Although this project does not focus on the detection of biosignatures, using μXRF to characterize geochemistry in a basaltic environment allows for a useful martian analog.

PIXL results are still relatively new, but one published paper, Hollis et al. (2022), discusses the utility of μXRF on fine grains. The minimum spot size is 120 μm on PIXL, while this project uses 20 μm. The finer spot size allows for greater detail into coarse and fine grains. This project found that using μXRF on loose sediment gives the ability to observe geochemistry within grain boundaries. Using PIXL for this purpose would not be useful for grain sizes less than 100 um due to the resolution causing the mix of mineral phases and blurring grain boundaries (Hollis et al., 2022). However, PIXL contains the resolution to analyze monomineralic versus multimineralic sediment in coarser grains and pebbles.

Multiple mineral phases, such as olivine, pyroxene, sulfates, halite, phosphate, and carbonates, were identified through PIXL and SHERLOC in Jezero rocks (Hollis et al., 2022). Through element maps in this project, olivine, pyroxene, and plagioclase mineral phases were identified in sediment. This indicated that the same techniques used on martian rocks can be applied to martian sand to further characterize sediment geochemistry through transport medium and distance from the source. Additionally, this project found weight percentages more useful for understanding how sediment changes geochemically with increasing grain size and distance from the source than using primarily element maps. As PIXL looks at sediment on Mars, this may also be useful.

5. CONCLUSIONS

μXRF was used to collect geochemical data on basaltic sediment in order to characterize the geochemistry with increasing distance from the source and through grain size fractions. The two glacial outwash fields in this study are composed of similar basaltic geology. The Kverkfjöll glacial outwash is characterized by glass dominated sediments, enriched in TiO_2, while the Þórisjökull glacial outwash is dominated by mineral or crystalline sediments suggested by the enrichment of Al_2O_3, MgO, and CaO. The findings of this project associate grain size, distance from source, source material, and transect length to controlling the geochemistry of the sand field. However, transport medium, such as aeolian or fluvial, did not have a notable effect on the geochemistry of basaltic sediment most likely due to the recycling of sediment in the system. Sediments from 2019 had a larger range of oxides in the finer fractions than in the coarse, indicating higher degrees of geochemical alteration occurs in the finer fractions. The 2021 sediments did not follow this same trend and usually had a larger range of oxide weight percentages, especially in the proximal site, suggesting either higher degrees of chemical weathering or a more complex geology in the area. Additionally, both field areas had similar geochemical trends with increasing grain size, yet differing trends with increasing distance from the source. This suggests that basaltic sediments typically have similar geochemical trends through grain sizes, however, geochemical trends with increasing distance from the source are dependent on the source material and transect length.

The μXRF produced weight percentages of oxides as well as element maps. The element maps, however, were not as useful for detecting geochemical trends through grain size and transport distance. Weight percentages were much better at depicting change through grain size

and distance from the source as they were quantitative measurements. The Fe, however, is underestimated in the grain size fraction of <63 um. The reason for the lack of utility in understanding geochemical trends is our project methodology analyzed multiple samples within one scan. The maps display geochemical fluorescence relative to what is in the scan and are therefore not comparable to other scans. Although the element maps were not useful for geochemical change, they allowed for the detection, and further investigation, of multimineralic versus monomineralic grains. Thin sections in this project revealed multimineralic grains typically reside in coarser fractions and are more relatable to source rock. The finer grains are typically monomineralic yet do have a small abundance of monomineralic grains. These differences are most likely related to physical abrasion and chipping of sediments as well as geochemical alteration. Transport medium, likewise, had no effect on the quantity of multi- versus monomineralic grains.

The conclusions found in this project are important implications for studying loose sediment on Mars. Results show that many variables, such as grain size, distance from source, source material, and transect length impact the composition of basaltic sediment, yet transport medium may not have a large impact. This is important as martian terrain has active aeolian processes, yet fluvial processes occurred long ago. µXRF allows for the detection of not only the detection of potential biosignatures in rocks, but reliable major and minor elements in sediment in a spatial way. The results of this project however show that µXRF is not as useful on loose sediment, but more impactful on rocks, floats and formations. µXRF on Mars can additionally aid in the understanding of multimineralic versus monomineralic minerals.

REFERENCES

Achilles, C. N., et al. "Mineralogy of an active eolian sediment from the Namib dune, Gale crater, Mars." *Journal of Geophysical Research: Planets* 122.11 (2017): 2344-2361.

Allwood, Abigail C., et al. "PIXL: Planetary instrument for X-ray lithochemistry." *Space Science Reviews* 216.8 (2020): 1-132.

Andronico, Daniele, et al. "Monitoring ash emission episodes at Mt. Etna: The 16 November 2006 case study." *Journal of Volcanology and Geothermal Research* 180.2-4 (2009): 123-134.

Arnalds, O., F. O. Gisladottir, and H. Sigurjonsson. "Sandy deserts of Iceland: an overview." *Journal of Arid Environments* 47.3 (2001): 359-371.

Arnalds, Olafur. "Volcanic soils of Iceland." *Catena* 56.1-3 (2004): 3-20.

Baratoux, David, et al. "Volcanic sands of Iceland-Diverse origins of aeolian sand deposits revealed at Kverkfjöll and Lambahraun." *Earth Surface Processes and Landforms* 36.13 (2011): 1789-1808.

Basdevant, Jean-Louis, and James Rich. "Fundamentals in nuclear physics: From nuclear structure to cosmology." *Springer Science & Business Media* (2005).

Bedford, C. C., et al. "Geochemical variation in the Stimson formation of Gale crater: Provenance, mineral sorting, and a comparison with modern Martian dunes." *Icarus* 341 (2020): 113622.

Bedford, C.C., et al. "The Role Of Glaciovolcanic Sources In Iceland's Mars-Analog Sedimentary Systems." *AGU Fall Meeting 2021* (2021).

Bedford C.C., et al. "Identifying the Products Of Volcano-Ice Interactions In The Martian Sedimentary Record." *53rd Lunar and Planetary Science Conference* (2022): Abstract #2844.

Bedford, C. C., et al. "Characterizing the Effects of Glaciation on the Volcanic Source Rocks of the SAND-E Mars-Analog Mission and Its Implications for Mars." *LPI Contributions* 2678 (2022): 2817.

Boggs, Sam. "Experimental study of rock fragments." *Journal of Sedimentary Research* 38.4 (1968): 1326-1339.

Brown, G. C., et al. "New light on caldera evolution—Askja, Iceland." *Geology* 19.4 (1991): 352-355.

Carr, Michael H. "The volcanoes of Mars." *Scientific American* 234.1 (1976): 32-43.

Carr, Michael H. "The fluvial history of Mars." *Philosophical Transactions of the Royal Society A: Mathematical, Physical and Engineering Sciences* 370.1966 (2012): 2193-2215.

Carrivick, Jonathan L., et al. "Palaeohydrology and sedimentary impacts of jökulhlaups from Kverkfjöll, Iceland." *Sedimentary Geology* 172.1-2 (2004): 19-40.

Catling, David C. "Mars atmosphere: History and surface interactions." *Encyclopedia of the solar system*. Elsevier, (2014): 343-357.

Champion et al. "μXRF Investigation of Geochemical and Physical Grain Characteristics in a Glacio-Fluvial-Aeolian Catchment in Southwest Iceland." *53rd Lunar and Planetary Science Conference (2022):* Abstract #2409.

Cornwall, Carin, et al. "Physical abrasion of mafic minerals and basalt grains: Application to martian aeolian deposits." *Icarus* 256 (2015): 13-21.

Crovisier, J-L., et al. "Dissolution of subglacial volcanic glasses from Iceland: laboratory study and modelling." *Applied Geochemistry* 7 (1992): 55-81.

Delvigne, Jean, et al. "Olivines, their pseudomorphs and secondary products." (1979): 247-309.

Edgett, Kenneth S., and Nicholas Lancaster. "Volcaniclastic aeolian dunes: Terrestrial examples and application to Martian sands." *Journal of Arid Environments* 25.3 (1993): 271-297.

Ewing R. C., et al. "Overview and Initial Results of SAND-E: Semi-Autonomous Navigation for Detrital Environments." *51st Lunar and Planetary Science Conference* (2020): Abstract #2857.

Fairén, Alberto G. "A cold and wet Mars." *Icarus* 208.1 (2010): 165-175.

Farley, Kenneth A., et al. "Mars 2020 mission overview." *Space Science Reviews* 216.8 (2020): 1-41.

Farley, K., et al. "Aqueously-altered igneous and sedimentary rocks on the floor of Jezero crater, Mars." *Science* (2022, accepted).

Fedo, Christopher M., Ian O. McGlynn, and Harry Y. McSween Jr. "Grain size and hydrodynamic sorting controls on the composition of basaltic sediments: Implications for interpreting Martian soils." *Earth and Planetary Science Letters* 423 (2015): 67-77.

Flude, Stephanie, Michael Haschke, and Michael Storey. "Application of benchtop micro-XRF to geological materials." *Mineralogical Magazine* 81.4 (2017): 923-948.

Fralick, Philip, and D. R. Lentz. "Geochemistry of clastic sedimentary rocks: ratio techniques." Geochemistry of Sediments and Sedimentary Rocks: Evolutionary Considerations to Mineral Deposit-Forming Environments: *Geological Association of Canada, Geotext* 4 (2003): 85-103.

Furman, Tanya, Peter S. Meyer, and Fred Frey. "Evolution of Icelandic central volcanoes: evidence from the Austurhorn intrusion, southeastern Iceland." *Bulletin of volcanology* 55.1 (1992): 45-62.

Ghatan, Gil J., and James W. Head III. "Candidate subglacial volcanoes in the south polar region of Mars: Morphology, morphometry, and eruption conditions." *Journal of Geophysical Research: Planets* 107.E7 (2002): 2-1.

Gíslason, Sigurður Reynir. "Weathering in Iceland." *Jökull* 58 (2008): 387-408.

Gudmundsson, Agust. "Infrastructure and mechanics of volcanic systems in Iceland." *Journal of Volcanology and Geothermal Research* 64.1-2 (1995): 1-22.

Goudge, Timothy A., et al. "Assessing the mineralogy of the watershed and fan deposits of the Jezero crater paleolake system, Mars." *Journal of Geophysical Research: Planets* 120.4 (2015): 775-808.

Goudge, Timothy A., et al. "Sedimentological evidence for a deltaic origin of the western fan deposit in Jezero crater, Mars and implications for future exploration." *Earth and Planetary Science Letters* 458 (2017): 357-365.

Goudge, Timothy A., et al. "Stratigraphy and paleohydrology of delta channel deposits, Jezero crater, Mars." *Icarus* 301 (2018): 58-75.

Goudie, A. S., and A. Watson. "The shape of desert sand dune grains." *Journal of Arid Environments* 4.3 (1981): 185-190.

Grotzinger, John P., et al. "A habitable fluvio-lacustrine environment at Yellowknife Bay, Gale Crater, Mars." *Science* 343.6169 (2014).

Hawley, Scott M., et al. "Continental weathering and terrestrial (oxyhydr) oxide export: comparing glacial and non-glacial catchments in Iceland." *Chemical Geology* 462 (2017): 55-66.

Hollis, Joseph Razzell, et al. "The power of paired proximity science observations: Co-located data from SHERLOC and PIXL on Mars." *Icarus* (2022): 115179.

Horgan, Briony HN, et al. "The mineral diversity of Jezero crater: Evidence for possible lacustrine carbonates on Mars." *Icarus* 339 (2020): 113526.

Hynek, Brian M., Michael Beach, and Monica RT Hoke. "Updated global map of Martian valley networks and implications for climate and hydrologic processes." *Journal of Geophysical Research: Planets* 115.E9 (2010).

Ingersoll, Raymond V., et al. "The effect of grain size on detrital modes: a test of the Gazzi-Dickinson point-counting method." *Journal of Sedimentary Research* 54.1 (1984): 103-116.

Jakobsson, Sveinn P., and Magnús T. Gudmundsson. "Subglacial and intraglacial volcanic formations in Iceland." *Jökull* 58 (2008): 179-196.

Jakobsson, Sveinn Peter. "Chemistry and distribution pattern of recent basaltic rocks in Iceland." *Lithos* 5.4 (1972): 365-386.

Jóhannesson, H., and K. Sæmundsson. "Geological map of Iceland. 1: 500.000. Bedrock." *Icelandic Institude of Natural History, Reykjavik* (1989).

Jónasson, Kristján. "Silicic volcanism in Iceland: Composition and distribution within the active volcanic zones." *Journal of Geodynamics* 43.1 (2007): 101-117.

Karhunen, Ritva. "Eruption mechanism and rheomorphism during the basaltic fissure eruption in Biskupsfell, Kverkfjoll, north-central Iceland." *Nordic volcanological institute* 8802 (1988).

Lo Castro, Maria Deborah, and Daniele Andronico. "Grain size distributions of volcanic particles by CAMSIZER." *Conferenza A. Rittmann*. 2009.

Mandon, L., et al. "Refining the age, emplacement and alteration scenarios of the olivine-rich unit in the Nili Fossae region, Mars." *Icarus* 336 (2020): 113436.

Mangold, N., et al. "Segregation of olivine grains in volcanic sands in Iceland and implications for Mars." *Earth and Planetary Science Letters* 310.3-4 (2011): 233-243.

Mangold, Nicolas, et al. "Chemical variations in Yellowknife Bay formation sedimentary rocks analyzed by ChemCam on board the Curiosity rover on Mars." Journal of Geophysical Research: Planets 120.3 (2015): 452-482.

Mangold, Nicolas, et al. "Fluvial regimes, morphometry, and age of Jezero crater paleolake inlet valleys and their exobiological significance for the 2020 Rover Mission Landing Site." *Astrobiology* 20.8 (2020): 994-1013.

Mangold, N., et al. "Perseverance rover reveals an ancient delta-lake system and flood deposits at Jezero crater, Mars." *Science* 374.6568 (2021): 711-717.

McDougall, Ian, Leo Kristjansson, and Kristjan Saemundsson. "Magnetostratigraphy and geochronology of northwest Iceland." *Journal of Geophysical Research: Solid Earth* 89.B8 (1984): 7029-7060.

McLennan, S. M., & Grotzinger, J. P. “The sedimentary rock cycle of Mars. In Jim Bell (Ed.), The Martian surface: Composition, mineralogy, and physical properties (Vol. 6).” *Cambridge University Press* (2008): 541–577.

Milton, Daniel J. "Water and processes of degradation in the Martian landscape." *Journal of Geophysical Research* 78.20 (1973): 4037-4047.

Moore, James G. "Vesicularity and CO_2 in mid-ocean ridge basalt." *Nature* 282.5736 (1979): 250-253.

Moore, James G., and Jean-Guy Schilling. "Vesicles, water, and sulfur in Reykjanes Ridge basalts." *Contributions to Mineralogy and Petrology* 41.2 (1973): 105-118.

Nahon, Daniel B., and F. Colin. "Chemical weathering of orthopyroxenes under lateritic conditions." *American Journal of Science* 282.8 (1982): 1232-1243.

Nanzyo, Masami. "Unique properties of volcanic ash soils." *Global Environmental Research-English Edition-* 6.2 (2002): 99-112.

Özdemir, Yavuz, Jon Blundy, and Nilgün Güleç. "The importance of fractional crystallization and magma mixing in controlling chemical differentiation at Süphan stratovolcano, eastern Anatolia, Turkey." *Contributions to Mineralogy and Petrology* 162.3 (2011): 573-597.

Pálmason, Gudmundur, and Kristján Sæmundsson. "Iceland in relation to the Mid-Atlantic Ridge." *Annual review of earth and planetary sciences* 2 (1974): 25.

Pokrovsky, O. S., et al. "Basalt weathering in Central Siberia under permafrost conditions." *Geochimica et Cosmochimica Acta* 69.24 (2005): 5659-5680.

Polacci, Margherita, et al. "Large vesicles record pathways of degassing at basaltic volcanoes." *Bulletin of Volcanology* 70.9 (2008): 1023-1029.

Powers, Maurice Cary. "A new roundness scale for sedimentary particles." *Journal of Sedimentary Research* 23.2 (1953): 117-119.

Rampe, Elizabeth B., et al. "Mineralogy and geochemistry of sedimentary rocks and eolian sediments in Gale crater, Mars: A review after six Earth years of exploration with Curiosity." *Geochemistry* 80.2 (2020): 125605.

Rollinson, Hugh Richard, Hugh Rollinson, and Victoria Pease “Using Geochemical Data: To Understand Geological Processes.” *Cambridge University Press* (2021).

Schon, Samuel C., James W. Head, and Caleb I. Fassett. "An overfilled lacustrine system and progradational delta in Jezero crater, Mars: Implications for Noachian climate." *Planetary and Space Science* 67.1 (2012): 28-45.

Schorghofer, Norbert, and Oded Aharonson. "Stability and exchange of subsurface ice on Mars." *Journal of Geophysical Research: Planets* 110.E5 (2005).

Sharp, Robert P., and Michael C. Malin. "Channels on mars." *Geological Society of America Bulletin* 86.5 (1975): 593-609.

Smellie, John L., et al. "Six million years of glacial history recorded in volcanic lithofacies of the James Ross Island Volcanic Group, Antarctic Peninsula." *Palaeogeography, Palaeoclimatology, Palaeoecology* 260.1-2 (2008): 122-148.

Stack, Kathryn M., et al. "Photogeologic map of the perseverance rover field site in Jezero Crater constructed by the Mars 2020 Science Team." *Space Science Reviews* 216.8 (2020): 1-47.

Stefánsdóttir, Matthildur B., and Sigurdur R. Gíslason. "The erosion and suspended matter/seawater interaction during and after the 1996 outburst flood from the Vatnajökull Glacier, Iceland." *Earth and Planetary Science Letters* 237.3-4 (2005): 433-452.

Storey, Michael, Richard G. Roberts, and Mokhtar Saidin. "Astronomically calibrated 40Ar/39Ar age for the Toba supereruption and global synchronization of late Quaternary records." *Proceedings of the National Academy of Sciences* 109.46 (2012): 18684-18688.

Suttner, Lee J. "Sedimentary petrographic provinces: an evaluation." (1974).

Thorpe, Michael "Basaltic Sediments from Source-to-Sink: Implications for the Paleoclimate of Mars." *Diss. State University of New York at Stony Brook* (2018).

Thorpe, Michael T., Joel A. Hurowitz, and Erwin Dehouck. "Sediment geochemistry and mineralogy from a glacial terrain river system in southwest Iceland." *Geochimica et Cosmochimica Acta* 263 (2019): 140-166.

Thorpe, Michael T., Joel A. Hurowitz, and Kirsten L. Siebach. "Source-to-sink terrestrial analogs for the paleoenvironment of Gale crater, Mars." *Journal of Geophysical Research: Planets* 126.2 (2021): e2020JE006530.

Tice, Michael M., Kimbra Quezergue, and Michael C. Pope. "Microbialite biosignature analysis by mesoscale X-ray Fluorescence (μXRF) mapping." *Astrobiology* 17.11 (2017): 1161-1172.

Tirsch, Daniela, et al. "Spectral and petrologic analyses of basaltic sands in Ka'u Desert (Hawaii)–implications for the dark dunes on Mars." *Earth Surface Processes and Landforms* 37.4 (2012): 434-448.

Varga, György, et al. "Saharan dust and giant quartz particle transport towards Iceland." *Scientific reports* 11.1 (2021): 1-12.

Veizer, Jan, and Siegfried L. Jansen. "Basement and sedimentary recycling-2: time dimension to global tectonics." The Journal of Geology 93.6 (1985): 625-643.

Villiger, Samuel, Peter Ulmer, and Othmar Müntener. "Equilibrium and fractional crystallization experiments at 0· 7 GPa; the effect of pressure on phase relations and liquid compositions of tholeiitic magmas." *Journal of Petrology* 48.1 (2007): 159-184.

Vingiani, S., F. Terribile, A. Meunier, and S. Petit (2010), Weathering of basaltic pebbles in a red soil from Sardinia: A microsite approach for the identification of secondary mineral phases, *Catena*, *83*(2-3), 96-106, doi:10.1016/j.catena.2010.07.001.

Walker, Angela Jane. "Rhyolite Volcanism At R Faj Kull Volcano, Se Iceland-A Window On Quaternary Climate Change." (2011).

Wordsworth, Robin D., et al. "Comparison of “warm and wet” and “cold and icy” scenarios for early Mars in a 3-D climate model." *Journal of Geophysical Research: Planets* 120.6 (2015): 1201-1219.

Yang, Junlong, C. WANG, and Zhenmin Jin. "Petrogenesis of high-Ti and low-Ti basalts: high-pressure and high-temperature experimental study." *AGU Fall Meeting Abstracts, Vol. 2017* (2017).

Young, Grant M., and H. Wayne Nesbitt. "Processes controlling the distribution of Ti and Al in weathering profiles, siliciclastic sediments and sedimentary rocks." *Journal of Sedimentary Research* 68.3 (1998): 448-455.

APPENDIX

Year	Sample	Grain Size (µm)	Grain Size Group	SiO_2	TiO_2	Al_2O_3	FeO	MnO	MgO	CaO	Na_2O	K_2O
2019	Proximal Aeolian	<63	Silt & Clay	NA	NA	NA	NA	NA	NA	NA	NA	NA
		63-125	Very Fine Sand	2.17E-03	1.59E-04	1.74E-03	3.42E-04	5.05E-05	1.69E-03	7.93E-04	2.75E-03	2.78E-04
		125-250	Fine Sand	1.70E-03	1.28E-04	1.33E-03	3.14E-04	4.52E-05	1.51E-03	6.01E-04	2.37E-03	2.40E-04
		250-710	Med. to Coarse Sand	3.37E-03	2.57E-04	2.64E-03	6.23E-04	8.60E-05	2.63E-03	1.18E-03	3.42E-03	1.35E-04
		710-1000	Coarse Sand	3.26E-03	2.42E-04	2.59E-03	5.81E-04	8.04E-05	2.49E-03	1.14E-03	3.33E-03	1.22E-04
	Proximal Fluvial	<63	Silt & Clay	5.66E-03	4.12E-04	4.38E-03	8.89E-04	1.32E-04	4.79E-03	2.04E-03	5.36E-03	2.35E-04
		63-125	Very Fine Sand	5.13E-03	3.82E-04	4.16E-03	8.63E-04	1.24E-04	2.35E-04	1.87E-03	5.11E-03	2.48E-04
		125-250	Fine Sand	4.26E-03	3.29E-04	3.35E-03	7.92E-04	1.10E-04	1.87E-03	1.50E-03	4.13E-03	2.06E-04
		250-710	Med. to Coarse Sand	3.78E-03	2.90E-04	2.95E-03	6.99E-04	9.67E-05	2.99E-03	1.32E-03	3.71E-03	1.52E-04
		710-1000	Coarse Sand	3.30E-03	2.49E-04	2.60E-03	6.00E-04	8.28E-05	2.59E-03	1.15E-03	3.31E-03	1.36E-04
	Medial Aeolian	<63	Silt & Clay	4.39E-03	3.34E-04	3.35E-03	7.02E-04	1.04E-04	3.91E-03	1.57E-03	4.48E-03	2.82E-04
		63-125	Very Fine Sand	5.38E-03	4.22E-04	4.34E-03	9.44E-04	1.34E-04	4.48E-03	1.90E-03	5.13E-03	2.65E-04
		125-250	Fine Sand	4.54E-03	3.64E-04	3.64E-03	8.60E-04	1.19E-04	3.72E-03	1.56E-03	4.33E-03	2.39E-04
		250-710	Med. to Coarse Sand	3.51E-03	2.71E-04	2.80E-03	6.51E-04	9.01E-05	2.70E-03	1.22E-03	3.46E-03	1.30E-04
		710-1000	Coarse Sand	3.60E-03	2.76E-04	2.87E-03	6.60E-04	9.08E-05	2.77E-03	1.26E-03	3.53E-03	1.39E-04
	Medial Fluvial	<63	Silt & Clay	6.42E-03	4.96E-04	4.96E-03	1.02E-03	1.51E-04	5.14E-03	2.31E-03	6.05E-03	3.07E-04
		63-125	Very Fine Sand	5.88E-03	4.90E-04	4.74E-03	1.03E-03	1.48E-04	4.44E-03	2.10E-03	5.61E-03	3.26E-04
		125-250	Fine Sand	4.58E-03	3.79E-04	3.64E-03	8.71E-04	1.23E-04	3.56E-03	1.59E-03	4.30E-03	2.58E-04
		250-710	Med. to Coarse Sand	3.89E-03	3.12E-04	3.07E-03	7.56E-04	1.03E-04	3.01E-03	1.37E-03	3.72E-03	1.41E-04
		710-1000	Coarse Sand	3.44E-03	2.73E-04	2.76E-03	6.50E-04	8.97E-05	2.55E-03	1.22E-03	3.40E-03	1.10E-04
	Distal Aeolian	<63	Silt & Clay	3.62E-03	2.90E-04	2.89E-03	5.35E-04	8.01E-05	2.84E-03	1.27E-03	3.79E-03	2.88E-04
		63-125	Very Fine Sand	4.30E-03	3.68E-04	3.50E-03	7.59E-04	1.09E-04	3.49E-03	1.49E-03	4.15E-03	2.49E-04
		125-250	Fine Sand	3.79E-03	2.87E-04	2.98E-03	7.35E-04	1.01E-04	2.49E-04	1.27E-03	3.61E-03	1.69E-04
		250-710	Med. to Coarse Sand	3.63E-03	2.81E-04	2.87E-03	6.85E-04	9.48E-05	2.98E-03	1.26E-03	3.53E-03	1.32E-04
		710-1000	Coarse Sand	3.41E-03	2.62E-04	2.69E-03	6.28E-04	8.72E-05	2.65E-03	1.19E-03	3.46E-03	1.31E-04
	Distal Fluvial	<63	Silt & Clay	6.71E-03	5.76E-04	5.22E-03	1.13E-03	1.64E-04	5.58E-03	2.29E-03	6.02E-03	3.48E-04
		63-125	Very Fine Sand	6.19E-03	5.11E-04	4.92E-03	1.18E-03	1.64E-04	5.50E-03	2.13E-03	5.61E-03	2.82E-04
		125-250	Fine Sand	4.97E-03	4.09E-04	3.92E-03	9.82E-04	1.36E-04	4.23E-03	1.69E-03	4.60E-03	2.59E-04
		250-710	Med. to Coarse Sand	4.52E-03	3.64E-04	3.52E-03	8.83E-04	1.22E-04	3.62E-03	1.58E-03	4.29E-03	1.89E-04
		710-1000	Coarse Sand	3.45E-03	2.74E-04	2.70E-03	6.60E-04	9.11E-05	2.73E-03	1.22E-03	3.37E-03	1.37E-04

Table 6. 2019 Error for Weight Percentage Data. 2 sigma, produced by the Bruker µXRF software.

Year	Sample	Grain Size (μm)	Grain Size Group	SiO_2	TiO_2	Al_2O_3	FeO	MnO	MgO	CaO	Na_2O	K_2O
2021	Proximal Aeolian	<63	Silt & Clay	3.90E-03	3.95E-04	2.68E-03	5.68E-04	8.50E-05	2.35E-03	1.03E-03	3.98E-03	4.46E-04
		63-125	Very Fine Sand	4.94E-03	6.01E-04	3.47E-03	1.10E-03	1.53E-04	2.99E-03	1.42E-03	4.69E-03	5.42E-04
		125-250	Fine Sand	4.55E-03	5.53E-04	3.27E-03	1.08E-03	1.47E-04	2.78E-03	1.32E-03	4.26E-03	4.72E-04
		250-710	Med. to Coarse Sand	3.94E-03	4.77E-04	2.85E-03	9.47E-04	1.28E-04	2.40E-03	1.14E-03	3.73E-03	4.09E-04
		710-1000	Coarse Sand	NA	NA	NA	NA	NA	NA	NA	NA	NA
	Proximal Fluvial	<63	Silt & Clay	5.06E-03	5.43E-04	3.31E-03	8.09E-04	1.21E-04	3.00E-03	1.36E-03	4.85E-03	5.92E-04
		63-125	Very Fine Sand	4.78E-03	5.70E-04	3.21E-03	1.01E-03	1.43E-04	2.86E-03	1.35E-03	4.58E-03	5.56E-04
		125-250	Fine Sand	4.53E-03	5.38E-04	3.08E-03	1.04E-03	1.43E-04	2.72E-03	1.27E-03	4.40E-03	5.12E-04
		250-710	Med. to Coarse Sand	3.63E-03	4.24E-04	2.43E-03	8.52E-04	1.17E-04	2.16E-03	9.87E-04	3.57E-03	4.15E-04
		710-1000	Coarse Sand	3.46E-03	4.00E-04	2.28E-03	8.21E-04	1.12E-04	2.00E-03	9.09E-04	3.44E-03	4.12E-04
	Medial Aeolian	<63	Silt & Clay	5.46E-03	5.72E-04	3.87E-03	9.48E-04	1.35E-04	3.63E-03	1.68E-03	5.10E-03	4.85E-04
		63-125	Very Fine Sand	5.31E-03	5.82E-04	3.90E-03	1.11E-03	1.53E-04	3.56E-03	1.70E-03	4.78E-03	4.35E-04
		125-250	Fine Sand	4.98E-03	5.30E-04	3.64E-03	1.11E-03	1.54E-04	3.43E-03	1.58E-03	4.57E-03	4.04E-04
		250-710	Med. to Coarse Sand	4.26E-03	4.35E-04	3.08E-03	9.49E-04	1.29E-04	3.01E-03	1.32E-03	3.93E-03	3.15E-04
		710-1000	Coarse Sand	3.83E-03	4.06E-04	2.71E-03	9.19E-04	1.24E-04	2.73E-03	1.14E-03	3.69E-03	3.23E-04
	Medial Fluvial	<63	Silt & Clay	5.58E-03	5.69E-04	3.96E-03	8.86E-04	1.27E-04	3.68E-03	1.66E-03	5.14E-03	5.00E-04
		63-125	Very Fine Sand	5.47E-03	6.07E-04	4.07E-03	1.16E-03	1.60E-04	3.67E-03	1.76E-03	4.71E-03	4.43E-04
		125-250	Fine Sand	5.04E-03	5.43E-04	3.76E-03	4.07E-03	1.53E-04	3.42E-03	1.64E-03	4.38E-03	3.88E-04
		250-710	Med. to Coarse Sand	4.39E-03	4.43E-04	3.27E-03	9.58E-04	1.30E-04	3.03E-03	1.43E-03	3.81E-03	3.02E-04
		710-1000	Coarse Sand	3.83E-03	4.06E-04	2.71E-03	9.19E-04	1.24E-04	2.73E-03	1.14E-03	3.69E-03	3.23E-04
	Distal Aeolian	<63	Silt & Clay	5.57E-03	6.10E-04	3.74E-03	1.01E-03	1.43E-04	4.07E-03	1.73E-03	5.95E-03	5.23E-04
		63-125	Very Fine Sand	5.68E-03	6.26E-04	3.88E-03	1.15E-03	1.59E-04	4.05E-03	1.77E-03	6.07E-03	5.21E-04
		125-250	Fine Sand	4.87E-03	5.15E-04	3.42E-03	1.01E-03	1.37E-04	3.44E-03	1.52E-03	5.26E-03	4.21E-04
		250-710	Med. to Coarse Sand	4.46E-03	4.53E-04	3.10E-03	9.19E-04	1.25E-04	3.18E-03	1.38E-03	4.69E-03	3.72E-04
		710-1000	Coarse Sand	3.47E-03	3.52E-04	2.35E-03	7.40E-04	1.00E-04	2.38E-03	1.05E-03	3.85E-03	3.57E-04
	Distal Fluvial	<63	Silt & Clay	5.80E-03	6.05E-04	3.87E-03	9.37E-04	1.36E-04	4.01E-03	1.76E-03	6.08E-03	5.62E-04
		63-125	Very Fine Sand	5.96E-03	6.61E-04	4.06E-03	1.20E-03	1.67E-04	4.19E-03	1.87E-03	6.41E-03	5.54E-04
		125-250	Fine Sand	5.19E-03	5.67E-04	3.58E-03	1.09E-03	1.49E-04	3.65E-03	1.63E-03	5.62E-03	4.71E-04
		250-710	Med. to Coarse Sand	4.77E-03	5.19E-04	3.27E-03	1.03E-03	1.40E-04	3.35E-03	1.48E-03	5.19E-03	4.31E-04
		710-1000	Coarse Sand	3.50E-03	3.41E-04	2.36E-03	7.05E-04	9.69E-05	2.30E-03	1.04E-03	3.62E-03	3.51E-04

Table 7. 2021 Error for Weight Percentage Data. 2 sigma, produced by the Bruker μXRF software